LAWRENCE
LIVERMORE
NATIONAL
LABORATORY

LLNL-JRNL-866447

Assessing the fidelity of shallow-water carbonates as records of the Ni isotope composition of surface seawater

E. J. Baransky, D. S. Hardisty, J. M. Rolison, L. E. Wasylenki

July 8, 2024

Geochimical et Cosmochimia Acta

Disclaimer

ASSESSING THE FIDELITY OF SHALLOW-WATER CARBONATES AS RECORDS OF THE NI ISOTOPE COMPOSITION OF SURFACE SEAWATER

Revisions submitted to

Geochimica et Cosmochimica Acta

May 29, 2025

Eva J. Baransky[1], Dalton S. Hardisty[2], John M. Rolison[3], Laura E. Wasylenki[1]

[1]School of Earth & Sustainability, Northern Arizona University, Flagstaff, AZ, USA 86011
[2]Department of Earth and Environmental Sciences, Michigan State University, East Lansing, MI, USA
[3]Nuclear and Chemical Sciences Division, Physical and Life Sciences Directorate, Lawrence Livermore National Laboratory, 7000 East Avenue, Livermore, CA, 94551, USA

Corresponding author: E. J. Baransky; ejb382@nau.edu

ABSTRACT

Nickel is a bioessential metal that is used in enzymes important to the C, N, and O cycles, and changes in its marine abundance and bioavailability may have affected the evolutionary trajectory of early life. Changes over time in the Ni isotope composition (δ^{60}Ni) of surface seawater, which reflects biological demand for Ni, could allow for the reconstruction of the dynamics of Ni demand over Earth's history, but this approach would require geologic records of surface seawater. Here, we investigate the fidelity of shallow-water carbonates as a record of the Ni isotope composition of surface seawater by determining how Ni is first partitioned into natural carbonates and then how post-depositional processes influence the Ni signal. Our samples come from the Great Bahama Bank, which is a well-studied, modern carbonate platform often used to study ancient platforms. We found that Ni is fractionated from seawater upon incorporation into carbonates capturing shallow (<18 cm), recent deposition (0.1‰ to 0.4‰ lighter than seawater). Variation among these [Ni] and δ^{60}Ni values may be controlled by variation in mineral proportions. Meteoric diagenesis shifts δ^{60}Ni to lower values, which we attribute to isotopically light meteoric fluids. In contrast, carbonates that experienced sediment-buffered marine diagenesis with respect to Ca isotopes and Sr/Ca ratios do not appear to differ in δ^{60}Ni values from sediments generally representative of their initial deposition. The sensitivity of δ^{60}Ni to diagenetic reset in these samples appears comparable to the sensitivities of Ca isotopes and Sr/Ca ratios, to first order. Thus, in general, carbonates that experienced sediment-buffered marine diagenesis with respect to these elements may hold the most promise as a record of the δ^{60}Ni of coeval surface seawater. Additionally, we use our results to infer that the fraction of Ni removed from seawater into carbonates is less than 10% of the total Ni output from the global oceans and incorporation of this Ni sink into global biogeochemical models will only have a minor impact on the modeled modern Ni budget.

KEYWORDS: nickel isotopes, carbonate diagenesis, nickel marine budget, Great Bahama Bank carbonates

1 Introduction

The co-evolution of Earth and life has resulted in some of the most profound changes in our planet's history (*e.g.,* oxygenation, long-term climate changes). We know few details about how the dynamic relationship between Earth's surface conditions and life operated during pivotal time periods because quantitative reconstruction of crucial element cycles in the distant past is extremely challenging. Much work has focused on reconstructing the cycling of macronutrients, such as C, N, and P, but the bioavailability of certain trace metals was likely similarly important. Specifically, trace metals are crucial components of the enzymes that enable use of

60 macronutrients (*e.g.,* Anbar and Knoll, 2002; Dupont et al., 2010; Glass and Orphan, 2012;
61 Robbins et al., 2016; Zerkle et al., 2006). More comprehensive knowledge of the dynamic
62 relationships between the atmosphere, oceans, and biosphere requires development of tools for
63 reconstructing the cycles of bioactive trace metals.

64 One trace metal that has almost certainly fluctuated from replete to limited bioavailability over
65 geologic time is Ni. Nickel is crucial to several biological processes in the C, N, and O cycles,
66 including N fixation, C acquisition as CO, and methanogenesis (Alfano and Cavazza, 2020;
67 Glass and Dupont, 2017; Ragsdale, 2009, 1998 and references therein). A substantial change in
68 Ni bioavailability may favor some organisms and inhibit others, due to varied Ni requirements.
69 For example, N-fixing cyanobacteria and methanogens have particularly high Ni demands (e.g.,
70 Diekert et al., 1981; Glass and Dupont, 2017; Ho, 2013; Nuester et al., 2012; Schonheit et al.,
71 1979), while certain flagellates need less and even find high Ni abundances to be toxic (Oliveira
72 and Antia, 1986; Twining et al., 2012). Furthermore, fluctuations in marine Ni concentrations
73 have likely affected the evolution of marine ecology and played a role in global redox and
74 climate events (*e.g.,* Great Oxidation Event: Konhauser et al., 2009, 2015; S.-J. Wang et al.,
75 2019; Snowball Earth events: S.-J. Wang et al., 2019; Zhao et al., 2021; Permian-Triassic
76 extinction: Rothman et al., 2014; Li et al., 2021). Thus, we need reliable tools for interpreting
77 geochemical signatures of Ni supply and demand dynamics as we aim to more thoroughly
78 reconstruct critical intervals of Earth-life history.

79 Ideally, we could quantify supply and demand for Ni by taking advantage of biological isotope
80 fractionation. For example, biological Cd uptake produces an isotopic composition in surface
81 seawater that is a function of nutrient supply (from deep seawater), the degree of utilization, and
82 the fractionation imparted by organisms. Druce et al. (2022) leveraged these relationships to

83 infer supply and demand for Cd by reconstructing the isotope compositions of surface seawater
84 and deep seawater derived from geologic records. A similar approach could be applied for Ni but
85 requires: (1) information about how different Ni consumers fractionate Ni isotopes and (2)
86 records of the Ni isotope compositions of surface and deep seawater. In the modern oceans,
87 different Ni consumers appear to have different biological fractionation factors. In waters
88 dominated by diatoms, surface biota do not appear to fractionate Ni isotopes, and the Ni isotope
89 compositions of surface and deep seawater are identical (Cameron and Vance, 2014; R. M.
90 Wang et al., 2019; Archer et al., 2020; Yang et al., 2020; Lemaitre et al., 2022). However, in
91 waters dominated by cyanobacteria, surface biota do appear to fractionate Ni isotopes, and
92 surface seawater has a heavier Ni isotope composition than deep seawater (Takano et al., 2017;
93 Archer et al., 2020; Yang et al., 2020; Lemaitre et al., 2022). This suggests that comparing the Ni
94 isotope compositions of coeval surface and deep seawater over time can provide information
95 about Ni utilization and even constrain the identity of the dominant Ni consumers. One of the
96 remaining challenges to applying this tool is identifying sedimentary archives of the Ni isotope
97 composition of contemporaneous surface and deep seawater.

98 Progress towards identifying sedimentary Ni isotope archives has focused primarily on deep
99 seawater. Two previous studies proposed that organic-rich sediments may preserve the Ni
100 isotope composition of deep seawater (Ciscato et al., 2018; He et al., 2023). These authors
101 measured the Ni isotope compositions of authigenic Ni in modern organic-rich sediments from
102 productive upwelling regions. They found that, when corrected for detrital contributions, the Ni
103 isotope compositions of the sediments closely matched that of modern deep seawater and may
104 therefore serve as a direct record. Research into possible post-depositional alteration is

105 warranted, but, at present, organic-rich sediments from upwelling regions appear to be a
106 plausible record of the Ni isotope composition of deep seawater.

107 Here, we investigate the fidelity of shallow-water carbonates as a record of the Ni isotope
108 composition of surface seawater, as carbonates have several attributes that could make them an
109 appropriate sedimentary record. Carbonates have a wide temporal and spatial distribution and
110 may be used as an archive of shallow or deep seawater chemistry, as they precipitate in
111 abundance in both shallow and deep marine settings. Because carbonates already serve as a
112 record of ancient seawater for several other proxies (*e.g.,* $\delta^{13}C$, $\delta^{18}O$: Veizer et al., 1986; $\delta^{66}Zn$:
113 Pichat et al., 2003; $\delta^{53}Cr$: Gilleaudeau et al., 2016), they provide a valuable opportunity for
114 multi-proxy comparisons to further constrain global feedback mechanisms. Like other
115 sedimentary records, carbonates are susceptible to diagenetic alteration. Fortunately, others have
116 made significant advancements in detecting and characterizing diagenesis in carbonates that may
117 help us differentiate diagenetic and seawater signals (*e.g.,* Allan and Matthews, 1982; Banner
118 and Hanson, 1990; Swart, 2015; Ahm et al., 2018; Higgins et al., 2018; Oehlert and Swart, 2019;
119 Fantle et al., 2020; Lau and Hardisty, 2022; Smith et al., 2022; Fantle and Lloyd, 2025).

120 Before we can interpret the Ni isotope composition record in carbonates, we must first address
121 two questions. How do Ni isotopes initially partition upon incorporation into carbonates from
122 seawater, and how does diagenesis alter the primary Ni isotope signal? No previous studies can
123 adequately answer either question, although we briefly acknowledge work with tangential
124 relevance. The only Ni isotope measurements of natural carbonates are from carbonate-
125 containing, lagoonal muds (Ciscato et al. 2018), carbonates derived from riverine suspended
126 particulate matter (Revels et al., 2021), and a Permian dolomite standard (Wu et al., 2019), none
127 of which have been calibrated or applied for paleoceanographic purposes. One experimental

study examined Ni isotope partitioning between solution and growing calcite crystals (Alvarez et al. 2021), but their experiments were conducted at pH 6 and pCO_2 of 1 atm in a simpler solution than seawater. While their results are helpful context, the applicability to natural carbonates is not yet clear.

To address these goals, we analyzed the Ni isotope compositions of shallow-water carbonate sediments from various diagenetic regimes and stages from the Great Bahama Bank. The Great Bahama Bank is an extensively studied, modern carbonate platform often used as an analog for ancient, shallow-water carbonate platforms (*e.g.,* Eberli et al., 1997; Hardisty et al., 2017; Higgins et al., 2018; Kenter et al., 2001; Liu et al., 2019; Manfrino and Ginsburg, 2001; Melim et al., 2002; Swart and Melim, 2000; Swart and Oehlert, 2018; Wang et al., 2020). This location is thus particularly well suited for our purpose. To determine how Ni isotopes partition initially into carbonates from seawater, we compared the Ni isotope compositions of carbonates representing shallow, early burial (<18 cm) to inferred Bahamian seawater and to each other, keeping mineralogical variations and crystallographic controls in mind. We next investigated how Ni and its isotopes repartition upon further diagenetic alteration of these shallow carbonates by comparing their Ni compositions to carbonates from initially similar environments that have since undergone common diagenetic reactions (*e.g.,* meteoric or marine burial diagenesis and/or dolomitization). Finally, to better constrain the conditions that preserve or alter the seawater Ni signal, we performed simple modeling that simulates progressive diagenetic alteration and evaluated the sensitivity of Ni to alteration relative to established indicators of diagenesis (*e.g.,* $\delta^{13}C$, Sr/Ca and $\delta^{18}O$).

2 Samples and Methods

2.1 Sample Description

The sample set includes carbonates that approximate initial deposition (shallow sediment cores, < 18 cm) and a range of diagenetic regimes: meteoric and marine diagenesis (Clino core), and dolomitization (Unda core) (Fig. 1). During early marine diagenesis, less stable carbonate polymorphs (*i.e.,* high-magnesium calcite and aragonite) recrystallize or neomorphose into more stable forms (*i.e.,* low-magnesium calcite and dolomite). The composition of the diagenetic carbonate with respect to each element or isotope ratio is largely influenced by (1) the compositions of the precursor sediment and diagenetic fluid, (2) whether diagenesis is fluid-buffered (occurring towards the beginning of the fluid flow path with relatively unaltered diagenetic fluid) or sediment-buffered (occurring later in the flow path with a diagenetic fluid that has evolved in composition along the path), accounting for each element's or isotope ratio's unique susceptibility to alteration, and (3) the degree of alteration.. With this sample set, we can determine whether the water column Ni isotope signals are preserved in our least altered carbonates and characterize the influence of meteoric and marine diagenesis, as well as dolomitization.

2.1.1 Shallow, Bank-top Sediment Cores

Near-surface modern carbonates in the Great Bahama Bank region are most likely to represent initial deposition of shallow-water carbonates among our samples (Hardisty et al., 2017; Pogge von Strandmann et al., 2019; Romaniello et al., 2013; Zhang et al., 2017). Detailed information about their collection methods and sample locations may be found in Hardisty et al. (2017). The short cores are < 20 cm bank-top cores near the Little Darby and Lee Stocking Islands (labeled C1, C4, and C5) (Fig. 1). The short cores are composed of inorganic carbonates such as ooids,

grapestones, and peloids and contain mainly aragonite with secondary amounts of high-magnesium calcite (HMC) (Hardisty et al., 2017). Radiocarbon dating of ooids from the Great Bahama Bank, but not directly from our sediments, indicate that the short-core carbonates have formed over the past 3,000 years (Duguid et al., 2010).

2.1.2 Clino and Unda

Several authors have extensively reviewed the mineralogy, sedimentology, and diagenetic history of the Clino and Unda cores, so we provide only a brief summary here (*e.g.,* Eberli et al., 1997; Higgins et al., 2018; Kenter et al., 2001; Manfrino and Ginsburg, 2001; Melim et al., 2002, 1995; Murray et al., 2021; Swart et al., 2012; Swart and Melim, 2000; Swart and Oehlert, 2018). The Clino and Unda cores were retrieved from the platform interior of the western flank of the Great Bahama Bank (Fig. 1) (Swart and Melim, 2000). The Unda and Clino cores were recovered from approximately 10 meters below sea level to 442 and 662 meters below seafloor (mbsf), respectively, extending back to the late Miocene (Eberli et al., 1997; Swart and Melim, 2000).

Carbonate mineral proportions vary greatly in both cores. The majority of the Clino core is dominated by low magnesium calcite (LMC), but some intervals contain >50% aragonite (*e.g.,* ~200 mbsf to 350 mbsf) (Melim et al., 1995; Hardisty et al., 2017). Dolomite occurs as a secondary component, mostly below 350 mbsf. The section of interest in the Unda core contains significant amounts of dolomite (often nearly 100% between 275 mbsf and 350 mbsf).

The Clino core contains well documented aragonite-to-LMC neomorphism in contact with meteoric and marine fluids. During repeated sea-level changes in the Pleistocene, meteoric fluids infiltrated the upper portions of Clino, resulting in negative oxygen and carbon isotope excursions (Melim et al., 1995; Swart and Oehlert, 2018; Eberli et al., 1997). The C and O

isotopes simultaneously become heavier downcore from 90 mbsf to 180 mbsf which could represent progressive mixing of carbonates that had experienced meteoric and marine diagenesis. Alternatively, the increase in C and O isotope ratios may instead be produced by varying degrees of diagenetic alteration driven by higher rates of organic matter oxidation at the intersection of the phreatic and vadose zones (Swart and Oehlert, 2018). Deeper in the core, early and late marine burial diagenesis are the dominant diagenesis regimes (*e.g.,* marine hardgrounds, neomorphism, compaction; Eberli et al., 1997; Higgins et al., 2018; Melim et al., 2001). Variations in mineralogy at these depths represent combinations of diagenetic aragonite-LMC neomorphism but also variations in shelf-to-slope aragonite transport and deposition during sea level variations (Swart and Eberli, 2005).

We targeted samples in the massive dolomite zone in the Unda core (between ~275 and 305 mbsf). The dolomites formed from sediments that had previously experienced aragonite-to-LMC neomorphism (Swart and Melim, 2000). Dolomitization occurred near enough to the sediment-water interface for advective exchange between seawater and pore fluid (Swart and Melim, 2000; Higgins et al., 2018; Dellinger et al., 2020; Murray et al., 2021; Wang et al., 2021). Low I/Ca+Mg ratios indicate the dolomites experienced anoxic (or at least iodate reducing) conditions in their diagenetic history (Hardisty et al., 2017).

2.2 Sample Preparation and Purification

All reagents were prepared with high purity water (18.2 MΩ cm) and were either distilled in house or purchased and individually assessed for purity (see procedural blanks below). Plastic items were acid cleaned in 1 M HCl and then 3 M HNO_3 for 24 hours each before use. PFA vials were soaked in dilute detergent (Citranox) and acid-cleaned in 150 °C baths of 6 M HCl and then 8 M HNO_3, each for 8 hours.

Approximately 0.1 g to 1 g of each carbonate sample was dissolved in 40 mL of 1 M HNO_3 and allowed to react at room temperature overnight (following Chen et al. 2018). Additional acid was added as needed to ensure complete dissolution of carbonate monitored by CO_2 evolution. Samples were dried and redissolved in 0.1 M HNO_3. Residual, undissolved material was removed by centrifugation (4000 RPM for 10 minutes). Samples were aliquoted to achieve 75 to 360 ng of Ni. To correct for isotope fractionation during ion exchange chromatography and instrumental mass fractionation, the samples were spiked with a ^{61}Ni-^{62}Ni double spike. Samples were spiked to achieve the optimal sample:spike ratio of 36:64 determined by the double spike toolbox algorithm from Rudge et al. (2009). Sample and spike were heated and allowed to equilibrate overnight.

We purified samples using a sequential, three-step ion exchange chromatography procedure. In the first column, Ca and Mg were removed using Nobias PA-1 resin, following the protocol outlined in Yang et al. (2020). Approximately 0.6 mL of precleaned resin was loaded into a Bio-Spin® Chromatography Column. The resin was cleaned on the column by adding 5 mL each of 1 M HNO_3, water, and 0.05 M ammonium acetate (pH 6.0 ± 0.2). Samples were loaded onto the resin in 10 mL of 0.05 M ammonium acetate (pH 6.0 ± 0.2), and then the resin was rinsed with 5 mL of 0.006 M ammonium acetate (pH 6.0 ± 0.2). Nickel was eluted with 5 mL of 1 M HNO_3. In the second column, remaining Ca and Mg and many transition metals (*e.g.,* Mn, Fe) were removed following the protocol in Strelow (1990). Poly-Prep® Chromatography Columns were loaded with 0.8 mL of precleaned AG50W-X8 200-400 mesh resin. The resin was cleaned on the column using 6 mL each of 3 M HCl, water, and 3 M NH_4OH – 0.1 M diammonium citrate. Samples were loaded onto the resin in 6 mL of 3 M NH_4OH – 0.1 M diammonium citrate, and then, the resin was rinsed with 6 mL of water. Nickel was eluted in 6 mL of 3 M HCl. In the

241 third column, Zn, Cu, and any remaining Fe were removed using protocols based on Kraus and
242 Moore (1953). Poly-Prep® Chromatography Columns were loaded with 1.0 mL of precleaned
243 AG1-X8 100-200 mesh resin. The resin was cleaned and conditioned on the column using 8 M
244 HCl. Samples were loaded onto the resin in 2 mL of 8 M HCl and then an additional 4 mL of 8
245 M HCl was added. Nickel was immediately eluted and collected.

246 We determined whether the sample purities were adequate by comparing the Ni/element ratios
247 (Na, Mg, Ca, Mn, Fe, Zn, and Cu) to acceptable thresholds defined previously for our analytical
248 method (Spivak-Birndorf et al., 2018). Individual column protocols were repeated as needed to
249 isolate Ni. Procedural blanks were always < 3.5 ng and typically < 2 ng. Our Ni yields were
250 nearly always >80%, with a minimum yield of 48%, but perfect yields are not necessary for
251 double-spiked samples.

252 **2.3 Sample Analyses**

253 Major and trace element concentrations were measured using an Agilent 7900 quadrupole
254 inductively coupled plasma mass spectrometer (ICP-MS). Doubly charged ions and oxide
255 formation were monitored during instrument tuning using Ce^{++}/Ce^{+} and CeO/Ce and were below
256 3%. At least three calibrating standards were used for each run and sample element
257 concentrations were always bracketed by the calibrating standards. A multi-element internal
258 standard was used to account for beam intensity fluctuations during measurement. Beam
259 suppression was monitored by checking the percent recovery for the internal standard elements
260 and was always within the range of 80-120% of the original blank solution measurement.

261 Nickel isotope analyses were performed on a ThermoScientific Neptune Plus multi-collector
262 ICP-MS at Lawrence Livermore National Laboratory and on a Nu Plasma 3 multi-collector ICP-
263 MS at Northern Arizona University. On the Neptune, samples were introduced at a rate of 50 μL

min^{-1} using an Apex Omega and ESI introduction system (Sc-μ DX). A Jet sample cone and X-skimmer cone were used. Voltages for masses 57, 58, 60, 61, and 62 were measured for Fe and Ni in high-resolution mode at the low mass side of the peaks to avoid Ar oxide interferences on ^{57}Fe ($^{40}Ar^{16}O^{1}H$) and ^{58}Ni ($^{40}Ar^{18}O$). Isobaric interferences from Ca oxides can also intrude on Ni masses (*e.g.,* $^{44}Ca^{16}O$ on ^{60}Ni and $^{42}Ca^{16}O$ on ^{58}Ni). We tuned to minimize oxide formation, which was monitored using CeO/Ce, to 0.4% to 0.8% across the different run days. We modeled how interferences from a 100 ppb Ca solution would impact the Ni isotope composition for our run conditions (*i.e.,* 0.4% to 0.8% oxide formation rates). The Ni isotope composition increased by 0.07‰ which is at the edge of our analytical uncertainty. This value is likely an upper bound because post-chemical purification measurements of our samples indicate that they contained less than 100 ppb Ca. In addition, our measurements appear robust considering samples were repeatedly measured across different days with different oxide formation rates, and their Ni isotope compositions were consistent across runs. Samples and bracketing standards were run at a Ni concentration of 250 ppb. Each sample analysis was bracketed by a blank acid measurement, for background subtraction, and a bracketing standard (NIST SRM 986) spiked the same way as the samples.

For analysis on the Nu Plasma 3 multi-collector ICP-MS, samples were introduced using a Cetac Aridus II introduction system. Masses 57, 58, 60, 61, and 62 were measured for Fe and Ni in low-resolution mode. Tuning was performed to minimize oxide formation to below <0.1% by monitoring CeO/Ce. Samples were measured in the same manner as described above, except for the background correction which only occurred at the beginning of each run.

Data processing included a correction on the ^{58}Ni voltages for isobaric interference from ^{58}Fe using the monitored ^{57}Fe ion beam. Instrumental mass bias correction was performed using an

iterative, geometric approach to the double-spike equations as described in Siebert et al. (2001). Ni isotope compositions are reported relative to the Ni isotope standard NIST SRM 986 in ‰ using delta notation, where

$$\delta^{60}Ni = \left(\frac{\left(^{60}Ni/^{58}Ni\right)_{sample}}{\left(^{60}Ni/^{58}Ni\right)_{SRM\ 986}} - 1 \right) \times 1000.$$

We took several different approaches to monitoring the quality of the data. Standards and selected samples were measured using both instruments and yielded analytically indistinguishable results (as noted in Table 1 and below). The long-term reproducibility of repeatedly analyzing the Ni isotope standard NIST SRM 986 was δ^{60}Ni = 0.00 ± 0.06‰, n=283 on the Neptune and δ^{60}Ni = 0.00 ± 0.09‰, n=925 on the Nu Plasma 3. We also purified an aliquot of NIST SRM 986 alongside the samples and measured an average δ^{60}Ni = 0.03 ± 0.03‰, n=8. To determine the efficacy of the purification protocol, we prepared three aliquots of a secondary Ni standard (Ni AAS standard solution, Alfa Aesar Specpure, lot# 9178435): one without purification, one with purification, and one doped with Ca, Mg, Fe, Mn, and Zn and then purified. The samples were measured on the Neptune, and the average δ^{60}Ni of all three are analytically indistinguishable from each other measured (δ^{60}Ni = -0.43 ± 0.08‰, n=64; -0.44‰ ± 0.08‰, n=9; -0.42 ± 0.07‰, n=16, respectively). For comparison, repeated measurements of unprocessed Ni AAS on the Nu Plasma 3 yielded identical results (δ^{60}Ni = -0.44 ± 0.10‰, n=180). Finally, we purified and analyzed mixtures of NIST SRM 986 and Ni AAS (3:1, 1:1, 1:3). A linear regression of the expected versus the measured δ^{60}Ni for the mixtures produced a slope of 1.06 and an R^2 of 0.89. We also bulk digested, spiked, purified, and measured the Ni isotope composition of a plankton standard (BCR-414). The average δ^{60}Ni is -0.01 ± 0.15‰ and

matches well with previously reported values ($\delta^{60}Ni = 0.11 \pm 0.06‰$, Takano et al., 2017; $\delta^{60}Ni = 0.07 \pm 0.06‰$, Yang et al., 2020).

Table 1: Mineralogy, major and trace element and Ni isotope compositions of the short-core carbonates, and Clino and Unda core carbonates.

				Isotopic composition (‰)			Mineralogy (wt. %)[2]				Major and trace element concentrations (ppm)[3]								
Core	Name	Depth (mbsf)	Instrument[1]	δ^{60}Ni	2σ	N	Arag.	HMC	LMC	Dolo.	Mg	Al	Ca	Mn	Fe	Sr	Ni[4]	Ni/Al	$D_{Ni\text{-}Carbonate}$
Unda	360[a]	109.73	A	0.63	0.13	3	0	0	59.32	40.68	55650	108	339035	9.7	134	1313	0.89	0.004	9.27
	377'2"	114.96	A	1.52	0.14	2	8.62	0	51.31	40.07	26297	26	337784	7.2	115	1447	0.38	0.007	3.91
	450'6"	137.31	A	1.35	0.01	2	0	0	87.8	12.2	18572	34	363370	9.9	71	1075	0.3	0.004	2.86
	901'	274.62	A	0.77	0.04	3	0	0	38.11	61.89	60482	106	300891	13.4	99	376	2.37	0.01	27.69
	904'4"	275.64	A	0.89	0.16	3	0	0	64.1	35.9	57702	84	302821	11.8	117	373	1.13	0.006	13.07
	915'10"	279.15	A	0.83	0.02	3	0	0	39.7	60.3	73267	98	305832	11.1	82	396	1.2	0.006	13.8
	925'2"	281.99	B	0.52	0.07	3	0	0	0.65	99.35	129431	134	270178	13.4	128	272	2.36	0.008	30.61
	944'8"	287.93	B	0.87	0.07	2	0	0	31.69	68.31	95916	129	258328	11.4	120	304	2.86	0.01	38.8
	950'2"	287.93	A	0.73	0.45	3	0	0	0.51	99.49	132953	194	276755	15.6	210	262	5.36	0.013	67.95
	970'10"	294.88	AB	0.97	0.2	4	0	0	1.1	98.9	119228	33	240984	9.7	106	191	2.76	0.038	40.18
	990'3"	301.83	A	0.76	0.12	3	0	0	1.06	98.94	123912	40	250259	13.3	145	219	2.1	0.024	29.43
	1000'	304.8	AB	0.47	0.05	3	0	0	0	100	123359	33	243496	13.4	130	205	2.23	0.031	32.11
Clino	79.6	24.12	AB	1.01	0.08	3	47.68	0	52.32	0	1492	56	353469	2.7	51	4329	0.88	0.007	8.73
	90'	27.43	A	1.12	0.01	2	24.89	0	75.11	0							0.24		
	93'	28	B	1.2		1	0	0	0	0							0.4		
	110'6"	33.57	A	1.31	0.06	2	0	0	100	0	4492	163	323290	8.3	140	1343	0.99	0.003	10.71
	112'2"	33.68	A	1.18	0.05	2	0	0	100	0							0.33		
	123'5"	37.62	A	1.14	0.11	3	13.78	0	86.22	0	4843	53	363494	3.8	47	1832	0.39	0.003	3.75
	130'	39.62	B	1.11		1	0	0	100	0	2741	124	274613	5.9	52	990	0.69	0.003	8.87
	133'	40.54	A	0.86	0	2	9.52	0	87.53	2.94	3625	51	356965	4.3	75	1689	0.28	0.003	2.78
	171' 4"	52.22	B	0.76		1	0	0	100	0							0.21		

	207'2"	63.2	B	1.19	0.15	3	0	0	0	0	3587	19	319149	3.6	73	1289	0.3	0.007	3.35
	318'	97	B	1.04	0.05	2					4588	24	390828	5.2	134	1011	0.4	0.008	3.56
	361'	110.03	B	0.54		1	0	0	100	0							0.24		
	406' 5"	123.88	B	0.95	0.14	4	0	0	100	0	6400	23	387491	8.9	57	1634	0.3	0.006	2.7
	468	142.65	B	1.5	0.01	2	0	0	100	0	7165	6	310351	6.6	-	1278	0.5	0.038	5.62
	500'	152.4	A	1.67	0.01	2	9.84	0	86.79	3.37	11115	7	330671	6.8	0	1130	0.3	0.02	3.19
	590'8"	180.04	A	1.58	0.03	2	22.19	0	75.62	2.2	10899	20	354268	12.1	9	1629	0.46	0.01	4.51
	642'4.5"	195.79	A	1.67	0.01	2	88.51	0	11.49	0	4320	9	340985	4.1	22	6055	3.99	0.204	41.07
	673'4"	205.23	AB	1.33	0.04	4	39.11	0	60.89	0	5250	25	355737	2.6	37	2283	0.63	0.012	6.24
	703'	214.27	A	1.46	0.07	2	2.74	0	97.26	0							0.27		
	736'1"	222.53	B	1.24	0.06	4	18.56	0	79.9	1.55	7083	88	328777	4	32	3006	0.58	0.003	6.16
	752' 9.5"	228	B	1.39	0.22	5	15.85	0	84.15	0									
	764'3.5"	232.96	B	1.28	0.1	4	46.8	0	51.65	1.55	5790	56	332018	3.4	33	3689	0.81	0.007	8.57
	1005'5"	306.45	B	1.19	0.08	3	65.43	36.6	-2.02	0	4858	84	377380	4	145	6425	1.35	0.007	12.51
	1046'8"	319.02	AB	1.19	0.04	4	64.98	0	35.02	0	5527	92	365112	2.3	145	6207	1.61	0.008	15.47
	1078'	328.57	AB	1.32	0.06	4	72.83	0	26.22	0.96	6782	102	378693	3	189	6206	1.53	0.007	14.21
	1087'11"	331.6	A	1.32	0.14	3	84.5	0	14.08	1.42	5877	90	369280	2.4	171	8161	1.77	0.009	16.87
	1125'8"	343.1	A	1.21	0	2	51.81	0	47.62	0.57	6392	142	369874	3.7	205	6306	1.87	0.006	17.74
	1189	362.6	B	0.93		1	51.68	0	48.32	0	6179	570	374274	19.8	832	9891	2.8	0.002	26.24
	1214'10"	370.28	B	1.3	0.11	3	0	0	66.13	33.87	19524	101	322143	6	127	2229	1.11	0.005	12.04
	1229'6"	374.75	B	1.32	0.03	3	8.27	0	54.35	37.38	25560	140	340045	6.1	178	2664	1.7	0.006	17.59
	1241'	378.4	B	1.22		1	5.79	0	89.31	4.9	14543	159	401739	9.7	269	2802	1.53	0.004	13.37
	1248'7"	380.7	B	0.73	0.02	3	3.3	0	81.46	15.24	24431	469	345542	5.6	83	2849	0.87	0.001	8.88
	1262'4"	384.76	A	1.54	0.07	2	0	0	78.03	21.97	23807	120	372070	4.5	104	2630	0.36	0.001	3.36
Short Core - C1	C1 0_2	0.01	A	1.42	0.08	3	75.96	22.79	1.25	0	10337	238	390250	4.2	112	6677	0.85	0.002	7.67
	C1 2_4	0.03	A	1.27	0.06	4	92.86	6.61	0.53	0	12031	213	515969	4.2	102	9571	0.62	0.001	4.19
	C1 4_6	0.05	A	1.32	0.08	3	91.23	8.45	0.32	0	7971	166	337650	3.2	78	7048	0.54	0.002	5.65
	C1 8_10	0.09	A	1.29	0.09	2	87.7	12.04	0.26	0	9334		396926			6995	0.64		5.7

	C1 10_12	0.11	A	1.27	0.03	4	83.26	17.12	-0.38	0	8276	191	385451	2.7	68	7608	0.53	0.001	4.82
	C1 12_14	0.13	A	1.61	0.02	2	77.6	23.02	-0.62	0	8091	159	408612	2.3	50	6297	0.42	0.001	3.64
	C4 2_4	0.03	A	1.25	0.01	2	75.68	24.15	0.16	0	12081	210	365322	7.1	113	6225	1.24	0.003	11.94
	C4 6_8	0.07	A	1.44	0.07	2	81.54	16.61	1.85	0	9865	326	313951	7.2	131	19532	1.36	0.002	15.21
Short Core - C4	C4 10_12	0.11	A	1.43	0.17	5	63.98	30.65	5.36	0	11758	187	373689	6.9	113	6067	1.33	0.003	12.54
	C4 14_17	0.16	A	1.41	0.04	5	68.7	30.56	0.75	0	10404	199	360811	7.1	112	6278	1.22	0.003	11.84
	C4 17_20	0.19	A	1.45	0.03	3	74.75	24.81	0.44	0	11547	183	358443	6.0	95	5797	1.09	0.003	10.72
	C5 1_2	0.02	A	1.16	0.12	3	91.36	7.1	1.54	0	6615	200	479799	1.9	69	7715	0.36	0.001	2.63
Short Core - C5	C5 3_4	0.04	A	1.17	0.05	4	89.65	9.34	1.02	0	5762	235	448719	1.6	63	6667	0.31	0.001	2.4
	C5 5_6	0.06	A	1.15	0.09	3	91.44	6.84	1.73	0	6802	182	427971	1.8	61	7033	0.3	0.001	2.5
	C5 7_8	0.08	A	1.11	0.07	2	93.9	4.69	1.41	0	5762	189	404243	1.5	58	20647	0.31	0.001	2.68

1. A refers to samples measured on a Neptune MC-ICP-MS. B refers to samples measured on a Nu Plasma 3 MC-ICP-MS. AB refers to samples measured on both instruments.

2. Mineralogy data are from Melim et al. (1995) and Hardisty et al. (2017).

3. Element concentrations for Clino and Unda are from Liu et al. (2019).

4. Ni concentrations are calculated using the double-spike reduction.

312

3 Results

3.1 Shallow, Bank-top Sediment Cores

All Ni concentration and isotope data as well as mineralogy and major and trace element concentrations are presented in Table 1 and Figures 2, 3, and 4. The short cores, which record early carbonate deposition, have a range of [Ni] from 0.30 to 1.36 ppm with an average of 0.75 ± 0.40 ppm (1σ, Fig. 2). The δ^{60}Ni values range from 1.11 to 1.61‰ with an average of 1.31 ± 0.14‰ (1σ), which is lighter than inferred Bahamian seawater (1.4 - 1.7‰). In general, both [Ni] and δ^{60}Ni are more similar within a core than between cores. There are no obvious trends in isotopic compositions downcore, suggesting no significant alteration due to early oxidation of organic matter and that oxidation of organic matter is not an important contributor of Ni in these sediments. In addition, there is a strong correlation between δ^{60}Ni and 1/[Ni] (R^2 =0.81). Ni concentrations and δ^{60}Ni values both increase with higher proportions of HMC ([Ni]~HMC R^2 = 0.60 and δ^{60}Ni~HMC R^2 = 0.54).

3.2 Clino and Unda Cores

The Clino and Unda cores experienced meteoric and marine diagenesis and extensive dolomitization (Fig. 3). For the Clino core, Ni concentrations range from 0.21 ppm to 3.99 ppm with an average [Ni] = 0.93 ± 0.85 ppm (1σ). The range of δ^{60}Ni from the entire Clino core is 0.54‰ to 1.67‰, with lighter values commonly between 0 to 150 mbsf (meteoric diagenesis) and heavier values below 350 mbsf (marine diagenesis). For the Unda core, Ni concentrations range from 0.30 ppm to 5.36 ppm with an average [Ni] of 1.99 ± 1.38 ppm (1σ). The δ^{60}Ni values range from 0.48‰ to 1.52‰ and average 0.86 ± 0.31‰. Our few datapoints from outside of the massive dolomitization interval within Unda suggest a significant increase in δ^{60}Ni across the meteoric-marine diagenesis boundary at approximately 110 mbsf. The highest Ni concentrations and lowest δ^{60}Ni values are from the massive dolomitization interval.

4 Discussion

4.1 Possible influence of non-carbonate inclusions

In the first steps towards establishing the utility of carbonates as a record of $\delta^{60}Ni_{seawater}$, we must determine how Ni isotopes initially partition into carbonates from seawater and how early marine diagenesis influences the primary Ni signal. The shallow, bank-top carbonates and diagenetically altered carbonates from the Clino and Unda cores allow us to address these questions, provided we consider whether our bulk digests of the samples truly represent Ni hosted by carbonate minerals or by inclusions of silicate detrital matter or Fe or Mn oxyhydroxides. Fortunately, the matrices analyzed here are almost entirely carbonate material (Melim et al., 1995; Hardisty et al., 2017), but we considered other phases because carbonates are not very rich in Ni compared to the aforementioned phases.

To assess the influence of non-carbonate Ni, we determined whether the Ni content of our carbonates is as expected for Ni solely derived from carbonates by comparing the measured bulk distribution coefficients ($D_{Ni\text{-}carbonate} = [Ni]/[Ca]_{carbonate}/[Ni]/[Ca]_{fluid}$) for our samples to previously published distribution coefficients for natural and experimental carbonates. We used the Ni/Ca of nearby Atlantic surface seawater (2.9×10^{-7}; Archer et al., 2020; Lemaitre et al., 2022; Summerhayes and Thorpe, 1996) and the Ni/Ca measured in the carbonates (6.8×10^{-7} to 1.9×10^{-5}, Table 1) to compute a bulk distribution coefficient for each sample. Our calculated $D_{Ni\text{-}carbonate}$ and previously published $D_{Ni\text{-}carbonate}$ values are compiled in Table 2.

Table 2: Distribution coefficients for Ni and carbonates from previously published studies and this study.

	Sample Description	$D_{Ni\text{-}Ca}$	Reference
Natural Samples	Short cores, bulk, aragonite and HMC	3 to 15	This study
	Short cores, HMC endmember (see 4.3.2)	33 to 44	This study
	Short cores, aragonite endmember (see 4.3.2)	2	This study
	Clino, aragonite and LMC	3 to 41	This study

	Unda, dolomite	3 to 68	This study
	Riverine suspended particulate matter	3 to 30	Revels et al. (2021)
Experimental or Theoretical	Calcite	1.09 ± 0.36	Alvarez et al. (2021)
		2.00	Carlsson and Aalto (1998)
		0.8 to 6	Curti (1999)
		1.04 ± 0.11	Lakshtanov and Stipp (2007)
		3.47	Wang and Xu (2001)
		1.0 ± 0.5	Munsel et al. (2010)
	Aragonite	0.55	Böttcher and Dietzel (2010)
		0.00013	Brazier and Mavromatis (2022)
		2.88	Wang and Xu (2001)

Our $D_{Ni\text{-}carbonate}$ values for calcite and aragonite are somewhat higher than what previous theoretical and experimental studies would lead us to expect (Table 2), but generally consistent with Ni derived only from carbonates. The highest $D_{Ni\text{-}carbonate}$ values are from dolomite-rich samples within Unda and from HMC-rich samples in the short-core carbonates (Table 1 and 2). Distribution coefficients have not been determined experimentally for Ni in dolomite or HMC. Both can be expected to contain more Ni compared to aragonite or pure calcite, because Ni^{2+} can readily substitute for Mg^{2+}, and both are divalent cations with similar atomic radii (Shannon, 1976).

To further investigate the potential Ni contributions from detrital matter or Fe or Mn oxyhydroxides, we compared Ni concentrations and $\delta^{60}Ni$ to Mn, Fe, and Al concentrations. The results of these comparisons and corresponding discussion are detailed in the supplemental material, and a brief summary is given here.

The strongest correlations are observed for [Ni], $\delta^{60}Ni$, and [Mn] in the short cores, which both exhibit positive correlations (Fig. S2) and for [Ni] and [Fe] in the marine diagenesis section of Clino, which is positive (Fig. S5). For the short cores, we conclude that it is unreasonable for Mn-oxide inclusions to be a large source of Ni because of the relatively high Ni/Mn ratios of the

short-core carbonates compared to other Mn-rich sediments and because of the similar [Mn] between the short-core samples and other carbonates. In addition, the Mn/Ca ratios of our samples (2.5×10^{-6} to 1.7×10^{-5}) are generally consistent with calculated Mn/Ca ratios if the Mn is derived only from carbonate (5.0×10^{-7} to 3.5×10^{-5}) based on $D_{Mn\text{-}Ca}$ values for calcite (from 1 up to 70; Lorens, 1981; Pingitore et al., 1988; Dromgoole and Walter, 1990; Mills et al., 2021) and Mn concentrations of nearby seawater (5.1 ± 0.4 nM, n=4; Kelly et al., 2022). Alternatively, there could be another mechanism imparting the relationship, such as a mixture of minerals with distinct compositions (discussed in section 4.3.2). For the marine diagenesis section of Clino, the positive correlation between [Ni] and [Fe] suggests that Fe-oxide inclusions host a nontrivial amount of Ni in the bulk carbonate. Thus, we must consider how Fe-oxide hosted Ni may influence the δ^{60}Ni data and our interpretations. We find that the samples with lowest [Fe] (< 50 ppm, Fig. S6), which are most representative of the pure carbonate endmember, have δ^{60}Ni values (1.24‰ – 1.67‰) that do not differ much from samples with higher [Fe] (nearly all between 1.19‰ – 1.54‰). Importantly, because of the similarity between low and high [Fe] samples, our interpretations in section 4 are unaffected.

As a final measure, we considered whether our Ni isotope data are consistent with Ni derived only from carbonates based on previously published data. We have few relevant Ni isotope data from carbonates with which to contextualize our samples, but the data we do have suggest that our Ni isotope data are entirely in agreement with Ni derived only or mostly from carbonates. We specifically focus on comparing the isotope fractionation between carbonate and fluid of our samples to those reported in the literature because of the diverse array of fluids from which the carbonates precipitated. The short-core carbonates representing early deposition are generally skewed towards lighter δ^{60}Ni values relative to the inferred Bahamian seawater range (discussed

below in section 4.2, $\Delta^{60}Ni_{fluid\text{-}solid}$ from -0.21‰ to 0.59‰, where $\Delta^{60}Ni_{fluid\text{-}solid} = \delta^{60}Ni_{fluid} - \delta^{60}Ni_{solid}$), which is generally consistent with previous findings. Revels et al. (2021) measured the Ni isotope compositions of dissolved riverine Ni and of Ni associated with different phases within the riverine suspended particulate load. The carbonate phases within the suspended particulate loads consistently had lighter Ni than the coexisting water, with fractionation factors from dissolved Ni ranging from 0.2‰ to 1.6‰. Ciscato et al. (2018) measured $\delta^{60}Ni$ values from 0.0‰ to 0.6‰ in carbonate-rich, lagoonal muds. They did not measure coexisting fluids, so we cannot calculate an isotope fractionation. However, their measured, bulk $\delta^{60}Ni$ values may reflect inclusion of detrital matter, and thus are not comparable to our data, because their samples have Ni/Al ratios that are similar to the upper continental crust (~0.1‰, Cameron et al., 2009; Wu et al., 2019). An experimental study of Ni coprecipitated with calcite at different precipitation rates found a range of $\Delta^{60}Ni_{fluid\text{-}calcite}$ from 0.3‰ to 0.9‰, with higher $\Delta^{60}Ni_{fluid\text{-}calcite}$ corresponding to slower precipitation rates (Alvarez et al., 2021). Although we cannot eliminate the possibility of inclusions having been in some samples, the reasoning above gives us confidence to interpret our results as reflections of initial precipitation and diagenetic history of the samples.

4.2 Inferring the Ni isotope composition of Bahamian Seawater

To calculate the isotope fractionation between seawater and shallow-water carbonates, we must constrain the Ni isotope composition of Bahamian seawater. We did not measure Bahamian seawater, so we infer a plausible range of $\delta^{60}Ni$ values from measurements of seawater that are closest in latitude and depth to the carbonate coring sites, keeping in mind processes that control the Ni isotope composition of surface seawater. Bank-top waters in the study area are flushed with nearby Atlantic surface seawater (Zhang et al., 2017; Pogge von Strandmann et al., 2019). Low latitude, Atlantic surface seawater $\delta^{60}Ni$ values average 1.5 ± 0.1‰ (1σ, <500 mbsl) and increase with decreasing Ni concentrations due to biological activity (Archer et al., 2020;

Lemaitre et al., 2022). We expect this average value to be a lower bound on the true δ^{60}Ni of Bahamian seawater because all published low latitude Atlantic surface seawater samples with Ni concentrations <2.5 nM have δ^{60}Ni values >1.6‰ (Archer et al., 2020; Lemaitre et al., 2022), and published Ni concentrations from within 200 miles of our study area are low (2.1 ± 0.2 nM, 1σ, n=3, <1 mbsl; Kelly et al., 2022). In addition, we propose that 1.7‰ is a plausible upper bound on the δ^{60}Ni of Bahamian seawater; Ni is never fully depleted in surface seawater either because the remaining Ni pool is not biologically available (Archer et al., 2020) or because of nutrient co-limitations (John et al., 2022), and this remaining Ni pool is modeled to have a δ^{60}Ni ~1.7‰ (Archer et al., 2020; Lemaitre et al., 2022). Indeed, all measured low-latitude surface seawater δ^{60}Ni values converge to approximately 1.7‰ (Takano et al., 2017; Archer et al., 2020; Yang et al., 2020, 2021; Lemaitre et al., 2022). Thus, for the purposes of our discussion, we infer the modern Bahamian seawater δ^{60}Ni to be between 1.4‰ and 1.7‰.

There is no evidence to suggest that the Ni isotope composition of seawater has changed significantly since the time of our samples' depositions. As noted, radiocarbon dating of nearby ooids sediments suggest that the short, bank-top cores formed within the past 3,000 years (Duguid et al., 2010). The residence time of Ni in the oceans is on the order of 10,000 to 40,000 years (Sclater et al., 1976; Gall et al., 2013; Cameron and Vance, 2014; Little et al., 2020). The age of the short-core carbonates, representing early burial, is well within the residence time of Ni in the oceans, and thus the Ni isotope composition of seawater has not changed since the time of deposition. All carbonates measured here from the Clino and Unda cores originally precipitated within the past 5.3 my (Eberli et al., 1997). Core-to-rim transects of Fe-Mn crust cores have relatively constant δ^{60}Ni values for the past 10 Ma, which is consistent with constant seawater δ^{60}Ni values since carbonate deposition up to the modern day (Gall et al., 2013; Gueguen et al.,

2016). The δ^{60}Ni of seawater would have to change significantly over the past 5 mya to explain the range of 1‰ in δ^{60}Ni values of our carbonate sediments.

Importantly, our discussion comparing the δ^{60}Ni values of recently deposited and diagenetic carbonates is unaffected by the true Bahamian seawater δ^{60}Ni. All of our samples appear to have originally precipitated from the same or similar seawater δ^{60}Ni values. Thus, any differences in the measured δ^{60}Ni values are not due to differences in the δ^{60}Ni values of the primary fluids. Ni isotope measurements of carbonates and coeval seawater will certainly be important to conduct in the future to better constrain the exact isotope fractionation between carbonates and seawater. For now, our proposed range for Bahamian seawater appears reasonable, and the exact value is not needed for our discussion of the controls on Ni isotope partitioning during early deposition and subsequent diagenetic alteration of carbonate sediments.

4.3 Early Deposition

Given our best estimate of Bahamian surface seawater's δ^{60}Ni of 1.4‰ to 1.7‰, we can now compare that to the shallow, bank-top core samples, which are nearest to initial carbonate deposition among our samples, to estimate the fractionation factor when Ni is initially incorporated within sediments. We found that the δ^{60}Ni values are consistently isotopically lighter than seawater (1.31 ± 0.14‰, 1σ) indicating an average isotope fractionation of 0.1‰ to 0.4‰.

While the short-core carbonates closely represent primary precipitation, they may have experienced some early diagenetic alteration, and we must consider the potential influence of that on the δ^{60}Ni values. As recrystallization and neomorphism occurs in the sediment column, porewaters may shift in composition, which in turn could shift chemical signatures in sediments. Indeed, sulfate reduction lowers pH and increases H_2S in shallow pore fluids from other cores

near our study area (Romaniello et al., 2013; Kalderon-Asael et al., 2024), affecting trace element compositions and isotope ratios (*e.g.,* I/Ca+Mg and U isotopes; Romaniello et al., 2013; Hardisty et al., 2017). However, unlike these other elements, Ni is not redox-sensitive under environmental conditions and thus may be less sensitive to impacts from early diagenesis. Still, changes in Ni speciation could cause isotope partitioning among aqueous Ni species and influence the Ni isotope composition of recrystallized carbonates. In this case, we would expect that, as porewater becomes more sulfidic, diagenetic carbonates would become isotopically heavier because Ni sulfide species are lighter than all other dominant, inorganic aqueous Ni species, as determined by density functional theory (Fujii et al., 2014). Yet, we do not observe this trend in the δ^{60}Ni values of the short-core carbonates; we would expect H_2S and aqueous Ni sulfide complexes to increase with depth, but δ^{60}Ni values down-core do not very systematically with depth (Fig. 2A). In addition, density functional theory estimations suggest that the pH variability in porewaters from our study area (range of 7 to 8; Romaniello et al., 2013) would not induce significant changes in Ni speciation (modeled for oxygenated waters; Fujii et al., 2014). Even if the short-core sediments do not precisely represent pristine carbonate precipitates, the Ni isotope compositions of carbonates may be resistant to very early diagenetic processes, and thus the shallow bank-top cores appear to be a reasonable first approximation of initial deposition.

Unexpectedly, given that all the short cores likely originally precipitated from well-mixed seawater and experienced similar alteration, we observed small but resolvable isotopic variations among the cores (~0.5‰, Fig. 2A). Our eventual goal is to be able to infer δ^{60}Ni of ancient seawater from carbonates, so next we consider two options for the mechanism causing the core-to-core variation: different precipitation rates or different mineral proportions.

4.3.1 Does precipitation rate control initial fractionation from fluid?

Evaluating this hypothesis is very challenging due to scarcity of information. The precipitation rates for our samples are unknown, and only one previous study has examined the relationship between precipitation rates and isotopic fractionation for Ni. In that study, Alvarez et al. (2021) proposed that $\Delta^{60}Ni_{fluid\text{-}calcite}$ is highly sensitive to calcite precipitation rate, having observed a correlation in calcite-Ni coprecipitation experiments where slower precipitation rates corresponded to larger $\Delta^{60}Ni_{fluid\text{-}calcite}$ values. This experimental result may have limited applicability regarding our short-core samples representing early burial, which contain more aragonite than calcite, even though the calcite should have higher concentrations of Ni than aragonite. The experiments also occurred at pH 6.2, pCO_2 = 1 atm, and ionic strength fixed at 0.2 M, and the effects of these differences in conditions on Ni isotopic behavior are unknown. Nevertheless, we proceed with an attempt to determine whether precipitation rates could impart the variation observed in our data.

The available information suggests that the short-core samples and experimental samples of Alvarez et al. (2021) may have had comparable precipitation rates. Broecker and Takahashi, 1966 estimated that precipitation rates for the Great Bahama Bank ranged from $4x10^{-8}$ to $4x10^{-7}$ mol $CaCO_3$ m^{-2} s^{-1}. Rates in the Alvarez et al. (2021) experiments range from $5x10^{-9}$ to $1x10^{-7}$ mol $CaCO_3$ m^{-2} s^{-1}, so the faster growth experiments, which correspond to smaller fractionations, had rates overlapping those for the Great Bahama Bank carbonates. Using the relationship between calcite precipitation rate and isotopic fractionation presented in Alvarez et al. (2021), the range of precipitation rates in the Great Bahama Bank should correspond to $\Delta^{60}Ni_{fluid\text{-}solid}$ from -0.17 to 0.44‰. We observed $\Delta^{60}Ni_{seawater\text{-}carbonate}$ from -0.21‰ to 0.59‰, which overlaps

512 with our estimated range, suggesting that a similar relationship between precipitation rate and
513 isotopic fractionation might explain the variation we observed in the short cores.

514 We did not see, however, what we would expect for Ni partition coefficients if precipitation rate
515 controlled the isotopic composition of the shallow, bank-top carbonates. Precipitation rate
516 influences the apparent $D_{X\text{-}Ca}$ for a given trace metal (X) because, at slower rates, the apparent
517 $D_{X\text{-}Ca}$ should be closer to the equilibrium value, while, at faster rates, the apparent $D_{X\text{-}Ca}$ is
518 influenced by diffusion in solution and/or movement from the mineral surface to the bulk crystal
519 (Watson, 2004; DePaolo, 2011). For elements with equilibrium $D_{X\text{-}Ca}$ much smaller or much
520 larger than 1, the apparent $D_{X\text{-}Ca}$ will be highly rate-dependent, as observed for Mn and Sr, for
521 example ($\partial D_{Mn\text{-}Ca}/\partial \log R = 0.27$, $\partial D_{Sr\text{-}Ca}/\partial \log R = 0.25$, where R is the precipitation rate; Lorens,
522 1981). For elements with $D_{X\text{-}Ca}$ similar to 1, like Ni, the apparent $D_{X\text{-}Ca}$ should be relatively
523 unaffected by precipitation rate ($\partial D_{Ni\text{-}Ca}/\partial \log R = -0.04$ to 0.04, Alvarez et al., 2021; Lakshtanov
524 and Stipp, 2007). From the experimental study, we would therefore expect to see no correlation
525 or only very weak correlation between $\Delta^{60}Ni_{fluid\text{-}solid}$ and $D_{Ni\text{-}Ca}$, but a strong, negative correlation
526 between $\Delta^{60}Ni_{fluid\text{-}solid}$ and precipitation rate ($\partial \Delta^{60}Ni_{fluid\text{-}calcite}/\partial \log R = -0.58$, Alvarez et al., 2021).
527 Yet, we did observe a modest positive correlation between $\delta^{60}Ni$ and $D_{Ni\text{-}Ca}$ ($R^2 = 0.29$, or 0.89 if
528 points outside of 1σ of residuals from best-fit line are omitted; Table 1). The relationship
529 between $D_{Ni\text{-}Ca}$ and $\Delta^{60}Ni_{seawater\text{-}carbonate}$ is therefore more likely imparted by another mechanism.

530 **4.3.2 Is Ni uptake different among carbonate mineralogies?**

531 We hypothesize that differing proportions of minerals, such as aragonite and HMC, with distinct
532 [Ni] and $\delta^{60}Ni$ values, could explain the observed variation from between shallow, bank-top
533 cores. Others have found previously that trace elements exhibit distinct partition coefficients and
534 isotope fractionations among different, coexisting carbonate minerals (*e.g.,* Mg, Ca, and Li;

Marriott et al., 2004; Gussone et al., 2005; Saenger and Wang, 2014; Lau and Hardisty, 2022), and thus Ni and its isotopes may also partition differently depending on the carbonate mineral. Our short core carbonates contain 64 to 94 wt.% aragonite and 5 to 31 wt.% HMC (Hardisty et al., 2017), and we do observe broad correlations between [Ni], δ^{60}Ni, and aragonite content (Fig. 2A), suggesting that our samples may contain different proportions of two distinct mineral endmembers.

To assess our hypothesis, we tested whether the trends in our data can be reproduced by calculating conservative mixtures of aragonite and HMC endmembers. If we cannot fit a mixing model to the data, mineralogy is not likely a major control on the Ni composition of the short-core carbonates. Lau and Hardisty (2022) used a similar approach to test whether carbonate mineralogy is a major control on trace element and isotope compositions from the Clino and Unda cores. For our model calculation, we used the measured mineral proportions, [Ni], and δ^{60}Ni for each sample from the Bahamas short cores to calculate potential endmember compositions using singular value decomposition (Glover et al., 2012). The calculated [Ni] and δ^{60}Ni of the aragonite and HMC endmembers are 0.2 ppm and 0.7‰ and 3.6 ppm and 1.5‰, respectively. We then used the calculated δ^{60}Ni and [Ni] endmember values and the measured carbonate mineralogy to determine a simulated δ^{60}Ni for each sample. We observe the expected 1:1 linear relationship between simulated and measured δ^{60}Ni (Fig. 2B, Fig. S7, $R^2_{[Ni]} = 0.60$, $R^2_{\delta 60Ni} = 0.59$) indicating that our samples' [Ni] and δ^{60}Ni values can be explained largely as combinations of the two endmembers.

The endmembers we defined with our own data set appear reasonable because they roughly agree with the few constraints available in the literature. Theoretically and experimentally determined partition coefficients for Ni into aragonite or calcite are compiled in Table 2. While

558 previously published values of $D_{Ni\text{-}aragonite}$ are highly varied, they are generally smaller than $D_{Ni\text{-}calcite}$ (Table 2). Thus, the low [Ni] in our modeled aragonite endmember relative to calcite is
560 consistent with these previous observations.

561 Similarly, the Ni isotope compositions of our endmembers match our expectation for the relative
562 difference in Ni isotope composition between aragonite and calcite. For the endmember isotopic
563 compositions, we turn to isotope partitioning theory in the absence of any experimental studies
564 of $\delta^{60}Ni$ in calcite and aragonite precipitated from solutions like seawater. We do know that, at
565 equilibrium, heavier isotopes partition preferentially into mineral cation sites or dissolved species
566 with shorter, stiffer bonds or with lower coordination numbers (Schauble, 2004). In the absence
567 of direct information about Ni coordination geometry as a trace constituent in carbonate
568 minerals, we assume Ni^{2+} substitutes directly for Ca^{2+} in $CaCO_3$ as other metals of similar radius
569 and charge do (Reeder et al., 1999). The Ca-O bond lengths are longer in aragonite than calcite
570 (Ca-O in aragonite = 2.53 Å versus 2.36 Å in calcite; *e.g.,* Falini et al., 1998; Jarosch and Heger,
571 1986). The coordination number with oxygen atoms of Ni in calcite should be six. If Ni^{2+} does
572 substitute directly for Ca^{2+} in aragonite, the coordination number is nine. For these reasons, we
573 expect Ni in aragonite to be isotopically lighter than Ni in HMC, and this is what we observed in
574 our samples; short-core carbonates with higher HMC content have higher $\delta^{60}Ni$ values (fig. 2).
575 An important caveat is that Mg^{2+}, which is similar in ionic radius to Ni^{2+}, unexpectedly has a
576 shorter Mg-O bond length in aragonite than calcite (*e.g.,* Finch and Allison, 2007) and is
577 isotopically heavier in aragonite than calcite (summarized in Saenger and Wang, 2014). This
578 may be because Mg^{2+} fits poorly in a nine-fold site and may instead be bound at aragonite
579 surfaces or as nano-inclusions that differ structurally from aragonite (Finch and Allison, 2007).

We acknowledge that our dataset is small and that this method overfits the model to the data but, with the information at hand, we consider our hypothesis to be reasonable.

4.4 Influence of Diagenesis

While seawater composition and primary mineralogy may be the main factors governing the Ni isotope composition of primary shallow-water carbonates, they are certainly not the only factors to consider when attempting to infer the δ^{60}Ni of seawater from ancient carbonates. The Ni isotope compositions preserved in the geologic record likely reflect additional influences, such as diagenesis, that may overprint the primary signal. We explore the effects of different diagenetic processes in the next section.

4.4.1 Meteoric Diagenesis

During sea level changes, shallow-water carbonates are susceptible to episodes of subaerial exposure and meteoric fluid penetration that can drive carbonate phase changes and either add or subtract Ni from the sediments. These processes could very likely alter the Ni isotopic signature recorded in primary carbonates. In the section of the Clino core with meteoric alteration, extensive neomorphism has resulted in near complete conversion of aragonite to LMC (Melim et al., 2001, 1995, Fig. 3). The meteoric diagenesis sections of the Clino and Unda cores have a combined average Ni concentration of 0.47 ± 0.26 ppm (1σ), somewhat lower than the average of 0.75 ± 0.40 ppm in the short cores, which are assumed to represent what the Clino and Unda carbonates were like prior to meteoric diagenesis. The δ^{60}Ni values in the meteoric sections (range of 0.5‰ to 1.5‰ and average of 1.04 ± 0.26‰, 1σ) shift to lighter values relative to the short cores (range of 1.1‰ to 1.6‰ and average 1.31 ± 0.14‰, 1σ) (Fig. 3 and 4). To determine whether these differences are significant, we compared the values for [Ni] and δ^{60}Ni of carbonates that experienced meteoric diagenesis to those of the short cores using a multiple

603 pairwise comparison test (Tukey-Kramer). While the Ni concentrations are not significantly
604 different, δ^{60}Ni values are significantly different (95% confidence level; Fig. 4).

605 The carbonates in the meteoric diagenesis region may have adopted their lighter Ni isotopic
606 compositions while in contact with meteoric fluids, if such fluids are indeed isotopically light.
607 Unfortunately, no data are yet available for relevant fluids. Others have analyzed groundwater
608 from a lateritic regolith (Ratié et al., 2015) and from a basaltic aquifer (Takano et al., 2021), but
609 we consider these samples too dissimilar to be applicable here. A handful of rainwater and snow
610 Ni isotope measurements suggest meteoric waters are isotopically light (-0.8‰ to 0.8‰) relative
611 to seawater, but these values correlate tightly with indicators of heavy oil combustion and
612 therefore do not represent unpolluted meteoric water (Takano et al., 2021). Instead, we use rivers
613 as a reference for meteoric fluids. Measurements of δ^{60}Ni of dissolved riverine Ni vary
614 significantly, from 0.18‰ to 1.35‰, with an abundance-weighted average of 0.9‰ (Cameron
615 and Vance, 2014; Revels et al., 2021). Importantly, all Ni isotope measurements for rivers are
616 lighter than the inferred Bahamian seawater range, from which the short-core carbonates
617 precipitated (1.4‰ to 1.7‰), and thus diagenetic carbonates precipitated from meteoric fluids
618 should be isotopically lighter than those precipitated from seawater.

619 Ni concentration data also support this interpretation. We do not expect a significant difference
620 in Ni concentrations between carbonates precipitated from seawater and those precipitated from
621 meteoric fluids, because rivers typically have Ni concentrations between 1 and 15 nM (Gaillardet
622 et al., 2014; Cameron and Vance, 2014; Revels et al., 2021) that are comparable to nearby
623 seawater Ni concentration measurements (2.1 nM, from within 250 km of our study site; Kelly et
624 al., 2022) and Atlantic surface seawater (~2 nM; Cameron and Vance, 2014; Archer et al., 2020;
625 Lemaitre et al., 2022). As expected, there is not a statistically significant difference between the

626 Ni concentrations of the short-core carbonates and those influenced by meteoric diagenesis (Fig.
627 4). Taken together, we propose that meteoric diagenesis lowers δ^{60}Ni by contributing isotopically
628 light Ni from fluid but does not necessarily significantly alter the Ni concentration of the
629 diagenetic carbonate. Preliminary diagenetic modeling also supports this conclusion (discussed
630 in section 4.4.3).

631 **4.4.2 Marine Diagenesis**

632 Unlike the carbonates in the meteoric diagenesis section, most of the samples from the marine
633 diagenesis section (150 to 400 mbsf) match the Ni isotope compositions of the shallow, bank-top
634 carbonates nearest to initial deposition. Samples from the Clino core have an average [Ni] = 1.31
635 ± 0.95 ppm and δ^{60}Ni = 1.31 ± 0.23‰ (1σ), which are within uncertainties of the short-core
636 carbonate Ni compositions (0.75 ± 0.40 ppm and 1.31 ± 0.14‰, 1σ). Tukey-Kramer pair-wise
637 comparison tests indicate no significant differences for either δ^{60}Ni or [Ni] ($p > 0.05$ for both;
638 Fig. 4).

639 The degree of alteration is not homogeneous throughout this range, however. From 200 to 350
640 mbsf, there is a significant amount of preserved aragonite, indicating a mild extent of alteration,
641 unlike the meteoric diagenesis region of Clino, which experienced near complete aragonite-to-
642 LMC neomorphism (Fig. 3; Melim et al., 1995). Several diagenetic indicators suggest that the
643 chemical composition of the primary aragonite was retained (*e.g.,* light Ca isotope compositions,
644 heavy C isotope compositions, and high Sr/Ca ratios; Ahm et al., 2018; Higgins et al., 2018;
645 Melim et al., 1995). Samples from this section of the Clino core have an average [Ni] = 1.16 ±
646 0.59 ppm and δ^{60}Ni = 1.29 ± 0.09‰, which is again very similar to the compositions of the
647 short-core carbonates.

In contrast, samples from outside this well-preserved interval show signs of extensive alteration and sediment-buffered diagenesis for several common diagenetic indicators (150 to 200 mbsf and 350 to 400 mbsf), as evidenced by higher LMC content, presence of dolomite, lower Sr/Ca ratios, lighter C isotope compositions, and slightly heavier Ca isotope compositions (Melim et al., 1995; Ahm et al., 2018; Higgins et al., 2018). In support of this interpretation, Lau and Hardisty (2022) calculated endmember chemical compositions of primary aragonite/HMC, sediment-buffered LMC, and fluid-buffered dolomite with respect to several diagenetic indicators (*e.g.,* Ca isotope ratios, Sr/Ca ratios). They modeled the mixing of these minerals in the proportions of the Clino core and generally reproduced the measured Ca isotope compositions and Sr/Ca ratios, indicating that the Clino core experienced dominantly sediment-buffered diagenesis with respect to Ca isotope and Sr/Ca ratios (dolomite is typically <20% in the Clino core). Despite the greater extent of alteration compared to samples between 200-350 mbsf, samples from 150-200 and 350-400 mbsf have an average [Ni] of 1.46 ± 1.24 ppm and δ^{60}Ni of 1.33 ± 0.33‰, which is nearly identical to that found in the less altered region and the short-core carbonates.

Based on these observations, we can hypothesize that marine diagenesis, even where the degree of alteration is high, did not reset the Ni signature of the Clino core sediments. We can further hypothesize that diagenetic alteration was sediment-buffered with respect to Ni, as well as with respect to Ca isotopes and Sr/Ca ratios. If true, then perhaps carbonates in which Ca isotopes and Sr/Ca ratios indicate sediment-buffered diagenesis can reasonably be assumed to have Ni signatures reflecting sediment-buffered diagenesis, which would greatly aid the identification of carbonate sediments that preserve pre-diagenetic signatures.

The potential for Ca isotope and Sr/Ca ratios to indicate accurately whether certain carbonate samples have likely preserved original Ni signatures depends on whether Ni is more or less susceptible to reset than those diagenetic indicators and whether the transition from sediment- to fluid-buffered diagenesis for Ni occurs at approximately the same extent of alteration. A detailed explanation of why the boundary region between fluid- and sediment-buffered diagenesis is different for every element or isotope system is provided in Fantle et al. (2010) and Fantle and Lloyd (2025), as well as quantitative methods for determining relative susceptibility for various diagenetic indicators. For our purposes, the most important comparison to make is among the K_d values for the elements of interest (where $K_d = [\text{Element}]_{solid}/[\text{Element}]_{fluid}$). An element with a larger K_d (stronger partitioning of the element or isotope into the solid) will generally be less susceptible to reset by diagenetic fluid than an element with a lower K_d. To approximate the K_d for Ni, we can consider $D_{Ni\text{-}Ca}$ (Table 2) and assume our diagenetic system contains stoichiometric calcite in equilibrium with seawater which yields a K_d for Ni on the order of 10^3. This is similar to the K_d for Ca (10^3) and larger than the K_d for Sr (10^2; *e.g.,* Baker et al., 1982 and references therein; Huang and Fairchild, 2001; Tang et al., 2008). Thus, we expect Ni to behave similarly or be less sensitive to alteration relative to Sr and Ca, at least to first order. Importantly, our use of these diagenetic indicators to contextualize the diagenetic behavior of Ni isotopes appears reasonable.

We infer from our work on the Clino core that when marine diagenesis is mild enough that samples retain aragonite and have high Sr/Ca ratios, light Ca isotopes, and heavy C isotopes, those samples are likely to have retained Ni isotope signatures from early deposition. These signatures may also remain following moderate alteration that is predominantly sediment-buffered with respect to the noted diagenetic indicators.

4.4.3 Modeling the relative sensitivity of Ni to alteration during diagenesis

We can also explore what processes or conditions preserve primary Ni signatures by modeling how the Ni isotope composition and other diagenetic indicators change during diagenesis. As stated above, diagenetic indicators such as $\delta^{13}C$, Sr/Ca, $\delta^{44}Ca$, and $\delta^{18}O$ can indicate the likelihood of primary signal preservation for other elements based on their relative sensitivities to diagenetic overprinting at varying fluid-to-rock ratios. As a simplistic example, if an isotope ratio $^{n}X/^{m}X$ is less resistant to a specific type of alteration than $\delta^{18}O$ at a given fluid-rock ratio, then when $\delta^{18}O$ is reset after experiencing that type of alteration, $^{n}X/^{m}X$ is likely reset as well. Thus, we compared the influence of diagenesis on $\delta^{60}Ni$ to common diagenetic indicators by modeling the progressive alteration of fresh carbonate sediment.

Given the limited knowledge of the behavior of Ni in carbonates, we avoided more complex modelling approaches (such as recommended by Fantle and Lloyd, 2025) and instead opted for a simple model approximating a single diagenetic process (aragonite-to-calcite neomorphism in a fluid-buffered, open system; Banner and Hanson, 1990). This approach does not explicitly consider important aspects of diagenesis such as reaction rate or fluid evolution, but, for this first exploratory approach, it provides an interesting lens through which to consider our data.

In this model, our system is initially composed of fresh fluid and primary aragonite. We allow solid and fluid to equilibrate in terms of Ni partitioning and isotope exchange, and then we replace the altered fluid with fresh fluid for further equilibration with the sediment (now with a smaller proportion of aragonite). This was repeated until steady state was achieved with respect to the C isotope composition (*i.e.,* one of the signatures most resistant to diagenetic alteration). We track the cumulative fluid-to-rock ratio, N, defined as

716 $$\mathrm{N} = \#\ \text{of equilibration steps} \times \frac{F}{1-\mathrm{F}},$$

717 where F is the mass fraction of fluid in the system determined by the solid's and fluid's densities
718 and the solid's porosity.

719 Our model parameters are derived from the results presented here and from the literature. All
720 values and model parameters are listed in Table S1. We assumed the initial sediment had the
721 average [Ni] and δ^{60}Ni of the short-core carbonates. The marine and meteoric diagenetic fluids
722 are assumed to be similar to nearby Atlantic surface water and the global average for rivers,
723 respectively (Gaillardet et al., 2014; Cameron and Vance, 2014; Revels et al., 2021). We used
724 the distribution coefficient for Ni and calcite as reported in the literature (see Table 2) and
725 applied two isotope fractionation factors for Ni: the value described by Alvarez et al. (2021) as
726 most representative of equilibrium isotope fractionation between fluid and calcite (0.9‰) and the
727 average isotope fractionation between the measured short-core carbonates and the upper end of
728 the inferred Bahamian seawater δ^{60}Ni range (~0.4‰).

729 The modeled results generally reflect our measurements (*i.e.,* little to no change in δ^{60}Ni values
730 during marine diagenesis and lower δ^{60}Ni values after meteoric diagenesis relative to our shallow
731 bank-top core δ^{60}Ni values representing early deposition) and suggest Ni is moderately sensitive
732 to diagenesis relative to other systems (*e.g.,* more resistant than δ^{18}O, but less so than δ^{13}C).
733 Meteoric diagenesis results in lower δ^{60}Ni values than marine diagenesis, which reflects the light
734 δ^{60}Ni we infer for meteoric fluids (Fig. 5). Marine diagenesis modeled with the isotope
735 fractionation calculated from the short-core carbonates results in constant δ^{60}Ni, unchanged from
736 the short-core value. For all other scenarios, progressive alteration typically results in lower
737 δ^{60}Ni. The modeled δ^{60}Ni begins to deviate from the initial range of δ^{60}Ni around $N \sim 10^2$, which
738 is less sensitive to alteration than δ^{18}O and Sr/Ca, but more so than δ^{13}C. In addition, a previous

739 study performed a similar exercise for other trace constituents and redox sensitive elements (Lau
740 and Hardisty, 2022). In comparison, δ^{60}Ni is more sensitive to reset than U isotope ratios or Cr
741 isotope ratios, but less so than carbonate-associated sulfate concentrations, for example (*e.g.,*
742 deviation from primary occurs at $N_{\delta 238U} \sim 10^3$, $N_{\delta 53Cr} \sim 10^4$, $N_{CAS} < 10^1$ assuming oxic seawater
743 as the diagenetic fluid; Lau and Hardisty, 2022). This suggests that δ^{60}Ni is poorly rock buffered
744 during diagenesis in open systems (*i.e.,* easily changed at moderate fluid-to-rock ratios). Our
745 results are generally consistent with the δ^{60}Ni values of the meteorically altered portion of Clino,
746 which experienced diagenesis in a relatively open system. In this case, the Ni isotope
747 composition deviates from shallow, bank-top carbonates, presumably because the alteration fluid
748 had a significantly different δ^{60}Ni relative to seawater. As more information about Ni
749 incorporation into carbonates becomes available, we would greatly benefit from more realistic
750 models that track fluid evolution, extents of alteration, and styles of alteration (*i.e.,* fluid- versus
751 sediment-buffered diagenesis), as have been applied previously for other isotope systems (*e.g.,*
752 Ahm et al., 2018; Lau and Hardisty, 2022; Murphy et al., 2022; Holmden et al., 2024).

753 **4.4.4 Dolomitization**

754 The massive dolomite section of the Unda core provides an opportunity to evaluate how
755 dolomite formation, which is common in the rock record, influences or overwrites the precursor
756 sediment δ^{60}Ni. The dolomites contain some of the highest Ni concentrations (1.13 ppm to 5.36
757 ppm) and lowest δ^{60}Ni values in our sample set (0.48-0.76‰; Fig. 3 and 4), unlike the short-core
758 carbonates which are assumed to represent the precursor sediment. Such low δ^{60}Ni values
759 immediately suggest that dolomitization either strongly fractionated Ni while incorporating it
760 during mineral transformation or directly inherited isotopically light Ni, without fractionation,
761 from an isotopically light external source.

762 Seawater is one possible source of Ni; these dolomites very likely formed with a seawater-like
763 fluid in a relatively open system, with several elemental and isotopic ratios exhibiting fluid-
764 buffered conditions, as indicated by Sr concentrations (Swart and Melim, 2000) and multiple
765 isotope systems (*e.g.,* Ca, Mg, Li, S; Higgins et al., 2018; Dellinger et al., 2020; Murray et al.,
766 2021). Considering that enough seawater fluxed the sediments to reset the isotopes of a major
767 element like Ca, it is likely that seawater also delivered a significant amount of Ni and reset the
768 Ni isotopic composition. The heavy Ni isotope composition of seawater (1.3‰ to 1.7‰ Lemaitre
769 et al., 2022, and references therein) compared to the dolomite, however, would require very
770 strong Ni isotope fractionation during dolomite formation. For such a fractionation to occur,
771 assuming a close approach to equilibrium, the lattice site for Ni should have longer Ni-O bonds
772 and slower bond vibrations, and/or a larger coordination number than the aqueous species of Ni
773 that is directly incorporated into dolomite (most likely $Ni(H_2O)_6^{2+}$ or hydrated $NiCO_3^0$). While
774 we do not have direct measurements of the Ni-O bond length in dolomite, we can make
775 inferences based on the coordination environment of other cations that occupy the same
776 crystallographic site. Dolomite contains alternating layers of Ca and Mg octahedra. We expect
777 Ni to substitute more readily for Mg than Ca because Ni^{2+} (0.69 Å) is more similar in size to
778 Mg^{2+} (0.72 Å) than Ca^{2+} (1.00 Å) when octahedrally coordinated (Shannon, 1976). The Mg-O
779 bond length is ~2.08 Å (Reeder, 1983), which is at most 0.03 Å longer than the Ni-O bond length
780 for $Ni(H_2O)_6^{2+}$ (2.05 Å to 2.08 Å; Fujii et al., 2011, and references therein). Such a small
781 difference in bond length would not likely produce a ~1‰ difference in $\Delta^{60}Ni_{seawater\text{-}dolomite}$,
782 which is approximately the order of magnitude needed to be consistent with our observations.
783 The calculated reduced partition function ratios for several species of Ni in Fujii et al., 2011,

indicate a maximum fractionation of only ~0.7‰ between many possible aqueous species of Ni, including dissolved $NiCO_3(H_2O)_4^0$, which should be among the most isotopically heavy species.

If fractionation from seawater cannot produce the observed low $\delta^{60}Ni$ dolomite values, then perhaps Ni-rich inclusions such as Mn oxide particles could have been reductively dissolved during diagenesis, resulting in incorporation of their Ni into the dolomite. Wang et al. (2021) concluded that the redox conditions in these sediments were likely suitable for Mn-oxide reduction by comparing two redox proxies, I/Ca+Mg and carbonate-associated sulfate sulfur isotope ratios ($\delta^{34}S_{CAS}$). Iodate reduction occurs at approximately the same redox potential as Mn(III/IV), whereas sulfate reduction occurs at lower potential (Rue et al., 1997). In the massive dolomite section, low I/Ca+Mg ratios (Hardisty et al., 2017) but seawater-like $\delta^{34}S_{CAS}$ (Murray et al., 2021) suggested that the redox conditions during dolomitization were between iodate and sulfate reduction. Ni released during reductive dissolution could supply substantial amounts of isotopically light Ni. Mn-oxides are very Ni-rich (up to a few wt.%; Manheim and Lane-Bostwick, 1989), and recent analyses of Mn-rich sediments indicate light $\delta^{60}Ni$ (-0.8‰ to +1.0‰; Little et al., 2020; Gueguen and Rouxel, 2021; Fleischmann et al., 2023). As we would expect, [Mn] and [Ni] in this region have a positive correlation, but a weak one ($R^2 = 0.32$). We would also expect to see unusually high [Mn] for carbonates, but the [Mn] values are only slightly elevated (average [Mn] = 12.5 ppm; Liu et al., 2019). For comparison, the average Mn concentration for the short-core carbonates is 4.1 ppm and for the Clino core carbonates is 5.7 ppm. The weak correlation between [Mn] and [Ni] and low [Mn] tend to refute the possibility of light Ni inherited from Mn oxide inclusions but cannot rule it out entirely.

Data from the massive dolomitization section of Unda suggests that dolomite readily incorporates Ni from elsewhere and likely does not record the original chemical composition of

807 the precursor sediment. Interpretations of dolomite $\delta^{60}Ni$ are not recommended unless
808 independent information about external Ni sources is available.

809 4.5 Implications for the Marine Ni Budget

810 Our study is a step forward toward reconstructing Ni budgets for ancient oceans but can also
811 inform modeling of the modern marine Ni budget. Recent papers present highly discrepant
812 estimates of how much Ni is removed from the oceans globally into carbonates. Ni is buried with
813 carbonates in both the organic carbon fraction (*i.e.,* Ni within organic matter associated with
814 carbonates) or the inorganic carbon fraction (*i.e.,* Ni bound within carbonate minerals). Ciscato
815 et al. (2018) calculated the first Ni carbonate flux by multiplying the amount of organic carbon
816 buried with carbonates by the Ni/TOC ratio found in carbonate-rich lagoonal sediments (Table
817 3). They inferred from this calculation that carbonates account for only 0.1% to 7% of the total
818 Ni output. Alternatively, Alvarez et al. (2021) estimated the Ni output with the inorganic
819 carbonate fraction by multiplying the total amount of $CaCO_3$ buried each year by the Ni
820 concentration of carboniferous marine limestones (Table 3). Their estimate resulted in a much
821 larger value, making up 10% to 50% of the total Ni output.

822 **Table 3: Carbonate fluxes and Ni concentrations used to calculate the modern carbonate Ni**
823 **output.**

Source	Carbon fraction	Carbonate flux			Ni concentration			Total Ni flux (mol Ni/yr)
		Value	Unit	Ref.[a]	Value	Unit	Ref.[a]	
Ciscato et al. (2018) [a]	Organic	6.0×10^{12}	g C_{org}/yr	1	0.00014	ppm Ni/TOC %	2	1.4×10^{7}
Alvarez et al. (2021)	Inorganic	3.2 to 14.7×10^{13}	mol $CaCO_3$/yr	1,3,4,5,6	2.69	ppm Ni	7	1.5 to 6.7×10^{8}
This study	Inorganic	1.1 to 3.8×10^{13}	mol $CaCO_3$/yr	3, 8	0.74	ppm Ni	this study	1.4 to 4.8×10^{7}

1. Hedges and Keil, (1995); 2. Ciscato et al. (2018); 3. Milliman and Droxler, (1996); 4. Milliman et al. (1999); 5. Schneider et al. (2000); 6. Berelson et al. (2007); 7. Zhao and Zheng (2014); 8. Cartapanis et al. (2018) and references therein.
a. The output calculated for the organic fraction of carbonates only includes the organic output associated with carbonates and not with other sediments.

824 Our data provide a new opportunity to constrain the carbonate Ni output. We first calculated an
825 inorganic-carbon carbonate flux by multiplying the total $CaCO_3$ buried each year and the average
826 Ni concentration of the short-core carbonates, which most closely reflect initial precipitation

827 (Table 3). This produces an output of 1.4 to 4.8 x 10^7 mol Ni/yr. When combined with the
828 organic-associated flux from Ciscato et al. (2018), our new estimate yields a bulk carbonate flux
829 of 2.8 to 6.2 x10^7 mol Ni/yr. This estimate does not take into account that pelagic carbonates,
830 which make up half of the total $CaCO_3$ flux, may have a different average Ni concentration
831 (Milliman and Droxler, 1995; Schneider et al., 2000; Berelson et al., 2007; Cartapanis et al.,
832 2018; Hayes et al., 2021). Even so, in the context of the marine Ni budget, carbonates do not
833 appear to be a significant output. The bulk carbonate flux composes only 3% to 8% of the total
834 Ni output presented in Ciscato et al. (2018) and is less than half of the estimate proposed in
835 Alvarez et al. (2021).

836 Although an experimental study of Ni-calcite coprecipitation suggested that fractionation of Ni
837 isotopes during incorporation into carbonates may significantly influence the Ni isotope
838 composition of seawater (Alvarez et al., 2021), our data indicate the opposite. Having found that
839 experimentally grown calcite can be very light compared to solution ($\Delta^{60}Ni_{fluid\text{-}calcite} > 0.9‰$),
840 they proposed that removal of Ni to carbonates can exert significant leverage on the isotope
841 composition of seawater. However, our results suggest that primary or near-primary, shallow-
842 water carbonates (1.31‰ ± 0.14‰) are fractionated by approximately 0.1 to 0.4‰ from
843 coexisting seawater. Therefore, changes in carbonate deposition fluxes will not substantially
844 influence the Ni isotope composition of seawater.

845 5 Summary

846 Shallow-water carbonates are one of the most widespread and well-studied geologic archives of
847 ocean chemistry, but diagenetic alteration complicates their use as a record. To assess their use
848 as a record of the Ni isotope composition of surface seawater, we measured element

concentrations and the Ni isotope compositions of shallow, bank-top cores (<18 cm) and diagenetically altered carbonates from the Great Bahama Bank. We found that Ni is isotopically fractionated from seawater upon incorporation into carbonates that approximate initial deposition ($\Delta^{60}Ni_{fluid\text{-}sediment}$ on average between 0.1‰ to 0.4‰), and relative proportions of aragonite and calcite may dictate the primary $\delta^{60}Ni$, since isotopically heavier Ni is associated with higher proportions of calcite. Meteoric diagenesis alters the Ni isotope composition towards lighter values, which we conclude is because meteoric fluids are isotopically lighter than seawater. In contrast, we found that marine diagenesis does not appear to significantly alter the Ni signal imparted during deposition. We showed that the relative susceptibility of Ni signatures to diagenetic reset is approximately comparable to those for Ca isotopes and Sr/Ca ratios, such that carbonate samples in which those indicators point to preservation of the primary signal or sediment-buffered diagenesis likely also reflect the primary Ni signatures. Our work highlights the potential for shallow-water carbonates to serve as records of contemporaneous seawater, as long as the possible influence of diagenetic reset is first evaluated.

6 Acknowledgements

This investigation was supported by NASA Exobiology grant NNX11AH54G and NSF-OCE Chemical Oceanography grant 2148715 to Laura Wasylenki, as well as by a Geological Society of America Student Research grant awarded to Eva Baransky. A portion of this work was performed under the auspices of the U.S. Department of Energy by Lawrence Livermore National Laboratory under Contract DE-AC52-07NA27344 with release number LLNL-JRNL-866447. Hardisty was supported by NASA Exobiology grant 80NSSC22K1560. We thank three anonymous reviewers and Associate Editor Matthew Fantle for thoughtful comments that enabled us to improve our manuscript.

7 Appendix A. Supplementary Material

This material includes information on the influence of non-carbonate phases on the measured Ni concentration and isotope composition and model parameters for the exercise described in section 4.4.3.

8 Data Availability

Data are available through Mendeley Data at https://doi.org/10.17632/w22g2k4t2n.1.

9 Figures

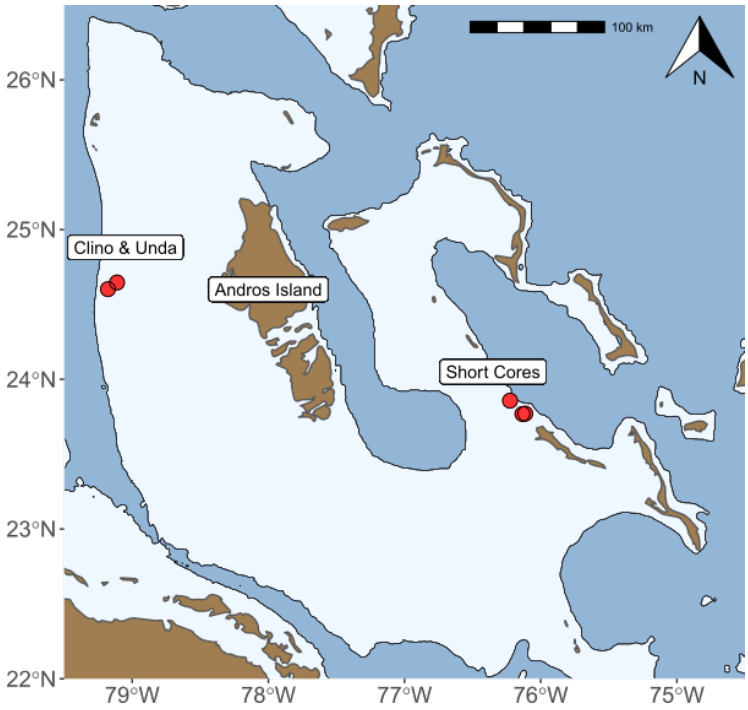

Figure 1: Sample Sites. Core locations are shown in red. Depths greater than 500 meters below sea level are shown in dark blue. Coordinate data are from Hardisty et al. (2017) and Ginsburg et al. (2001).

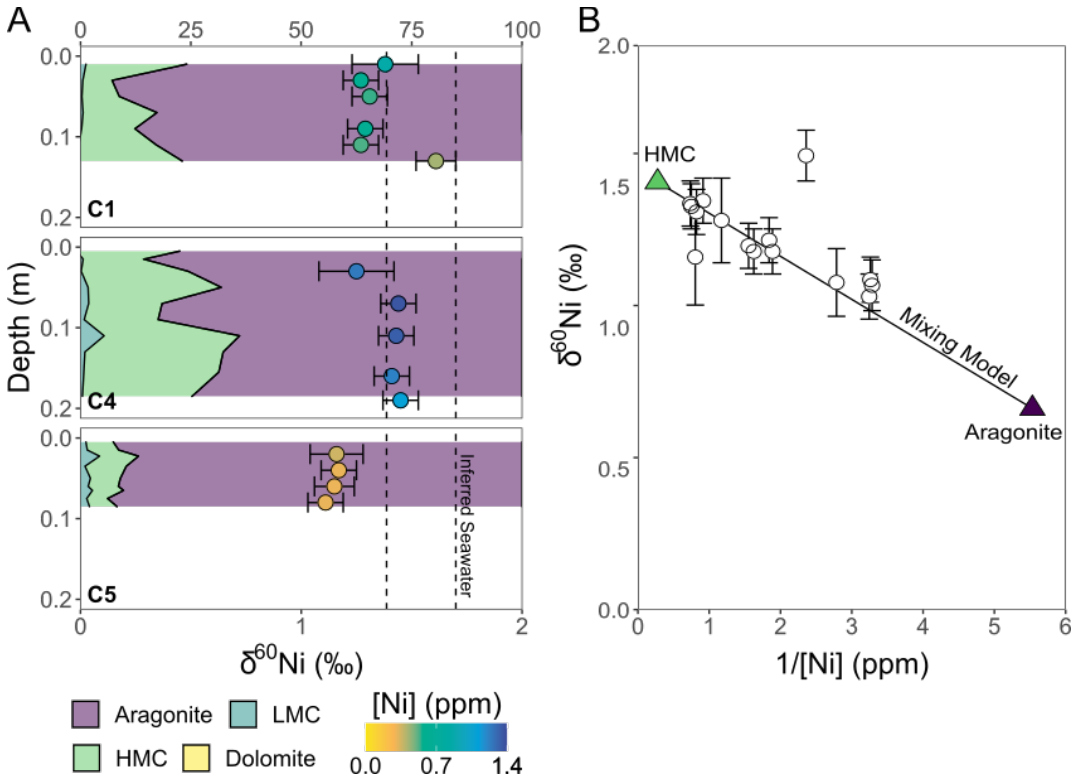

Figure 2: (A) Mineral proportions (colored fields), δ^{60}Ni (x-axis values), and [Ni] (color gradient) down short cores C1, C4, and C5. The two vertical dashed lines enclose the inferred Bahamian seawater δ^{60}Ni range as discussed in section 4.2. The mineralogy data are from Hardisty et al. (2017). The error bars represent 2σ on replicate analyses of the sample or 2σ on the long-term reproducibility for a Ni standard, whichever is greater. (B) depicts measured δ^{60}Ni and 1/[Ni] for the short-core carbonates (circles) and calculated δ^{60}Ni and 1/[Ni] values for aragonite and high-magnesium calcite endmembers (triangles, calculated as described in section 4.3.2). The black, solid line is the calculated mixing model from the two endmember compositions.

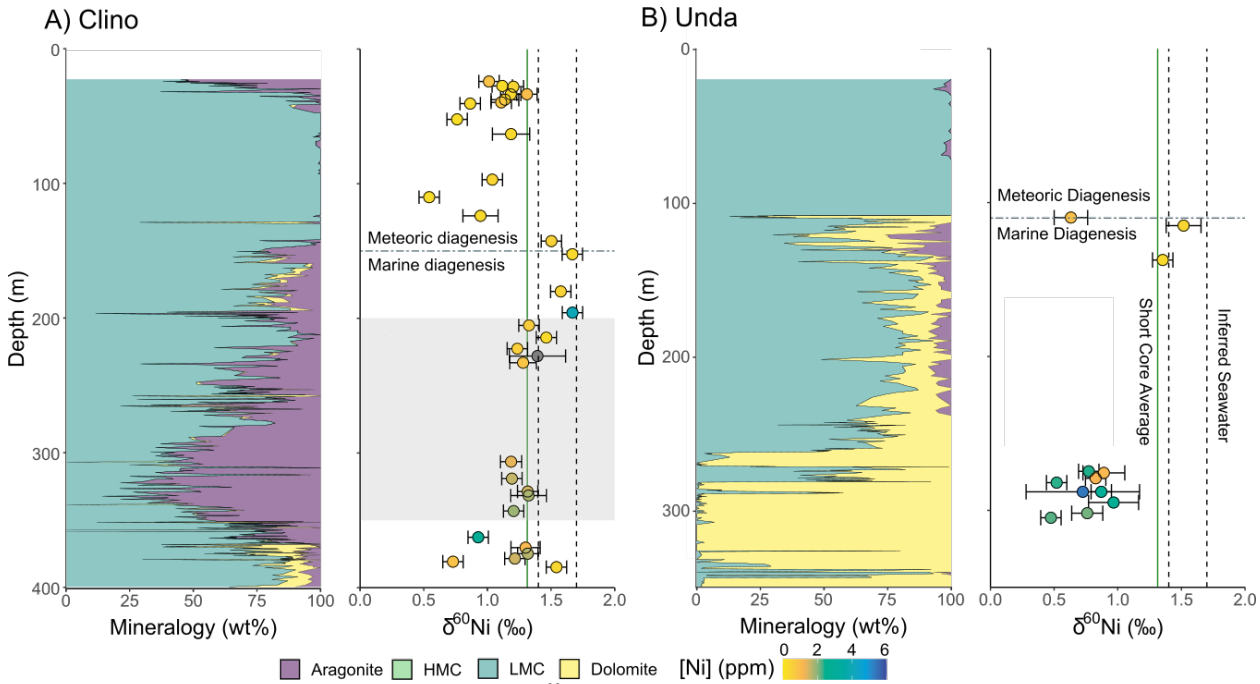

Figure 3: Mineral proportions, [Ni], and δ^{60}Ni values for Clino (A) and Unda (B). The green solid line corresponds to the average Ni isotope composition of the short-core carbonates. The two vertical dashed lines enclose the inferred Bahamian seawater δ^{60}Ni range as discussed in section 4.2. The horizontal, dash-dot line corresponds to the boundary between meteoric and marine diagenesis as defined by Melim et al. 2001, 1995. However, we acknowledge that meteoric fluids may have penetrated below this point (Swart and Oehlert, 2018). In panel A, the grey, shaded area denotes the region in which the sediments reflect the primary carbonate composition which suggests minimal alteration of the sediment (see section 4.4.2). Mineralogical data are from Hardisty et al. (2017) and Melim et al. (1995). The error bars represent 2σ on replicate analyses of the sample or 2σ on the long-term reproducibility for our Ni standard, whichever is greater.

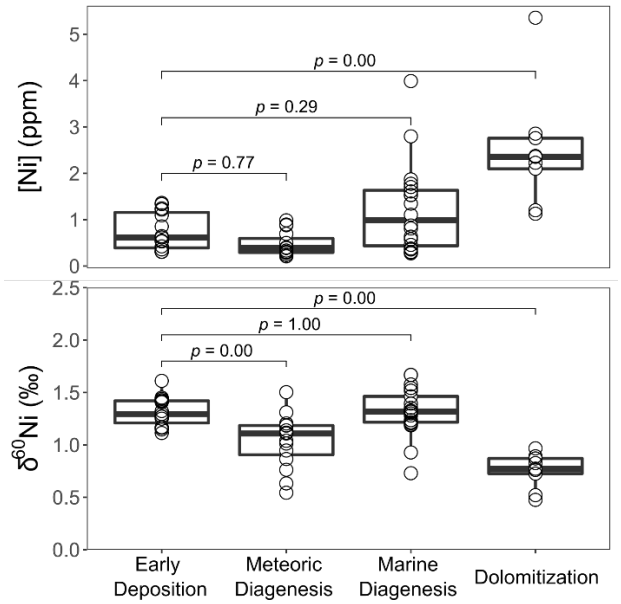

Figure 4: Comparison of [Ni] and δ^{60}Ni among primary or near primary and diagenetically altered carbonates for all cores. The results from a pairwise comparison test (Tukey-Kramer, which tests the null hypothesis that the population means do not differ for all pairs possible in the group) are shown to highlight the differences in [Ni] and δ^{60}Ni values of the shallow, bank-top carbonates which approximate initial deposition to that of carbonates that experienced further diagenesis.

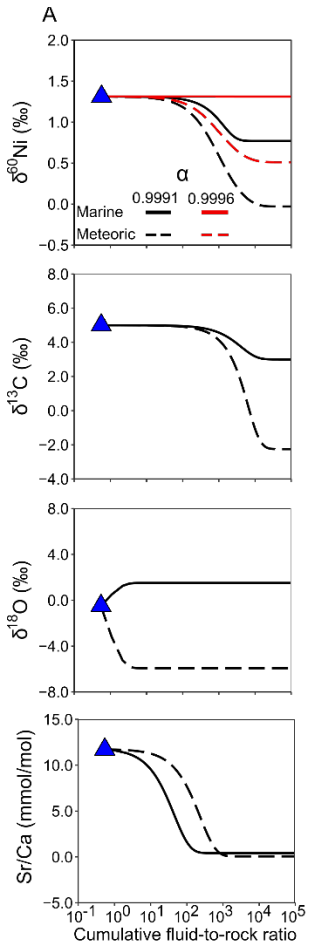

Figure 5: Diagenesis modeling results calculated as described in the section 4.4.3. The initial carbonate composition is shown as a blue triangle. Dashed lines correspond to diagenesis with meteoric fluids. Solid lines correspond to diagenesis with marine fluids. In the Ni isotope plot, black lines correspond to models using the Alvarez et al. (2021) equilibrium isotope fractionation of 0.9‰, whereas red lines correspond to the average isotope fractionation between short-core carbonates and the upper value of inferred Bahamian seawater (0.4‰). Model parameters are listed in supplementary Table S1.

10 References

Ahm A. S. C., Bjerrum C. J., Blättler C. L., Swart P. K. and Higgins J. A. (2018) Quantifying early marine diagenesis in shallow-water carbonate sediments. *Geochim. Cosmochim. Acta* **236**, 140–159.

Alfano M. and Cavazza C. (2020) Structure, function, and biosynthesis of nickel-dependent enzymes. *Protein Sci.* **29**, 1071–1089.

Allan J. R. and Matthews R. K. (1982) Isotope signatures associated with early meteoric diagenesis. *Sedimentology* **29**, 797–817.

Alvarez C. C., Quitté G., Schott J. and Oelkers E. H. (2021) Nickel isotope fractionation as a

function of carbonate growth rate during Ni coprecipitation with calcite. *Geochim. Cosmochim. Acta* **299**, 184–198.

Anbar A. D. and Knoll A. H. (2002) Proterozoic ocean chemistry and evolution: A bioinorganic bridge? *Science (80-.).* **297**, 1137–1142.

Archer C., Vance D., Milne A. and Lohan M. C. (2020) The oceanic biogeochemistry of nickel and its isotopes: New data from the South Atlantic and the Southern Ocean biogeochemical divide. *Earth Planet. Sci. Lett.* **535**, 116118.

Baker P. A., Gieskes J. M. and Elderfield H. (1982) Diagenesis of Carbonates in Deep-Sea Sediments - Evidence from Sr/Ca ratios and interstitial Dissolved Sr2+ Data. *J. Sediment. Petrol.* **52**, 71–82.

Banner J. L. and Hanson G. N. (1990) Calculation of simultaneous isotopic and trace element variations during water-rock interaction with applications to carbonate diagenesis. *Geochim. Cosmochim. Acta* **54**, 3123–3137.

Berelson W. M., Balch W. M., Najjar R., Feely R. A., Sabine C. and Lee K. (2007) Relating estimates of CaCO3 production, export, and dissolution in the water column to measurements of CaCO3 rain into sediment traps and dissolution on the sea floor:A revised global carbonate budget. *Global Biogeochem. Cycles* **21**, 1–15.

Broecker W. S. and Takahashi T. (1966) Calcium carbonate precipitation on the Bahama Banks. *J. Geophys. Res.* **71**, 1575–1602.

Cameron V. and Vance D. (2014) Heavy nickel isotope compositions in rivers and the oceans. *Geochim. Cosmochim. Acta* **128**, 195–211.

Cameron V., Vance D., Archer C. and House C. H. (2009) A biomarker based on the stable isotopes of nickel. *Proc. Natl. Acad. Sci. U. S. A.* **106**, 10944–10948.

Cartapanis O., Galbraith E. D., Bianchi D. and Jaccard S. L. (2018) Carbon burial in deep-sea sediment and implications for oceanic inventories of carbon and alkalinity over the last glacial cycle. *Clim. Past* **14**, 1819–1850.

Ciscato E. R., Bontognali T. R. R. and Vance D. (2018) Nickel and its isotopes in organic-rich sediments: implications for oceanic budgets and a potential record of ancient seawater. *Earth Planet. Sci. Lett.* **494**, 239–250.

Dellinger M., Hardisty D. S., Planavsky N. J., Gill B. C., Kalderon-Asael B., Asael D., Croissant T., Swart P. K. and West A. J. (2020) The effects of diagenesis on lithium isotope ratios of shallow marine carbonates. *Am. J. Sci.* **320**, 150–184.

DePaolo D. J. (2011) Surface kinetic model for isotopic and trace element fractionation during precipitation of calcite from aqueous solutions. *Geochim. Cosmochim. Acta* **75**, 1039–1056.

Diekert G., Konheiser U., Piechulla K. and Thauer R. K. (1981) Nickel requirement and factor F430 content of methanogenic bacteria. *J. Bacteriol.* **148**, 459–464.

Dromgoole E. L. and Walter L. M. (1990) Iron and manganese incorporation into calcite: Effects of growth kinetics, temperature and solution chemistry. *Chem. Geol.* **81**, 311–336.

Druce M., Stirling C. H., Bostock H. C. and Rolison J. M. (2022) Cadmium isotope systematics in sedimentary carbonate : Extending the utility of the cadmium isotope palaeo-productivity proxy. *Geochim. Cosmochim. Acta* **339**, 80–96.

Duguid S. M. A., Kurtis Kyser T., James N. P. and Rankey E. C. (2010) Microbes and ooids. *J. Sediment. Res.* **80**, 236–251.

Dupont C. L., Buck K. N., Palenik B. and Barbeau K. (2010) Nickel utilization in phytoplankton assemblages from contrasting oceanic regimes. *Deep. Res. Part I Oceanogr. Res. Pap.* **57**, 553–566.

Eberli G. P., Swart P. K., McNeill D. F., Kenter J. A. M., Anselmetti F. S., Melim L. A. and Ginsburg R. N. (1997) A Synopsis of the Bahamas Drilling Project: Results from Two Deep Core Borings Drilled on the Great Bahama Bank. *Proc. Ocean Drill. Program, 166 Initial Reports* **166**.

Falini G., Fermani S., Gazzano M. and Ripamonti A. (1998) Structure and morphology of synthetic magnesium calcite. *J. Mater. Chem.* **8**, 1061–1065.

Fantle M. S., Barnes B. D. and Lau K. V. (2020) The Role of Diagenesis in Shaping the Geochemistry of the Marine Carbonate Record. *Annu. Rev. Earth Planet. Sci.* **48**, 549–583.

Fantle M. S. and Lloyd M. K. (2025) Demystifying diagenesis: The future of diagenetic inquiry in the geosciences. In *Treatise on Geochemistry, 3e* pp. 249–314.

Fantle M. S., Maher K. M. and Depaolo D. J. (2010) Isotopic approaches for quantifying the rates of marine burial diagenesis. *Rev. Geophys.* **48**, 1–38.

Finch A. A. and Allison N. (2007) Coordination of Sr and Mg in calcite and aragonite. *Mineral. Mag.* **71**, 539–552.

Fleischmann S., Du J., Chatterjee A., Mcmanus J., Iyer S. D., Amonkar A. and Vance D. (2023) The nickel output to abyssal pelagic manganese oxides : A balanced elemental and isotope budget for the oceans. *Earth Planet. Sci. Lett.* **619**, 118301.

Fujii T., Moynier F., Blichert-Toft J. and Albarède F. (2014) Density functional theory estimation of isotope fractionation of Fe, Ni, Cu, and Zn among species relevant to geochemical and biological environments. *Geochim. Cosmochim. Acta* **140**, 553–576.

Gaillardet J., Viers J. and Dupré B. (2014) *Trace Elements in River Waters*.,

Gall L., Williams H. M., Siebert C., Halliday A. N., Herrington R. J. and Hein J. R. (2013) Nickel isotopic compositions of ferromanganese crusts and the constancy of deep ocean inputs and continental weathering effects over the Cenozoic. *Earth Planet. Sci. Lett.* **375**, 148–155.

Gilleaudeau G. J., Frei R., Kaufman A. J., Kah L. C., Azmy K., Bartley J. K., Chernyavskiy P. and Knoll A. H. (2016) Oxygenation of the mid-Proterozoic atmosphere: Clues from chromium isotopes in carbonates. *Geochemical Perspect. Lett.* **2**, 178–187.

Glass J. B. and Dupont C. L. (2017) Oceanic Nickel Biogeochemistry and the Evolution of Nickel Use. In *RSC Metallobiology* Royal Society of Chemistry. pp. 12–26.

Glass J. B. and Orphan V. J. (2012) Trace metal requirements for microbial enzymes involved in the production and consumption of methane and nitrous oxide. *Front. Microbiol.* **3**, 1–20.

Glover D. M., Jenkins W. J. and Doney S. C. (2012) Least squares and regression techniques, goodness of fit and tests, and nonlinear least squares techniques. In *Modeling Methods for Marine Science* pp. 49–74.

Gueguen B. and Rouxel O. (2021) The Nickel isotope composition of the authigenic sink and the diagenetic flux in modern oceans. *Chem. Geol.* **563**, 120050.

Gueguen B., Rouxel O., Rouget M. L., Bollinger C., Ponzevera E., Germain Y. and Fouquet Y. (2016) Comparative geochemistry of four ferromanganese crusts from the Pacific Ocean and significance for the use of Ni isotopes as paleoceanographic tracers. *Geochim. Cosmochim. Acta* **189**, 214–235.

Gussone N., Böhm F., Eisenhauer A., Dietzel M., Heuser A., Teichert B. M. A., Reitner J., Wörheide G. and Dullo W. C. (2005) Calcium isotope fractionation in calcite and aragonite. *Geochim. Cosmochim. Acta* **69**, 4485–4494.

Hardisty D. S., Lu Z., Bekker A., Diamond C. W., Gill B. C., Jiang G., Kah L. C., Knoll A. H., Loyd S. J., Osburn M. R., Planavsky N. J., Wang C., Zhou X. and Lyons T. W. (2017) Perspectives on Proterozoic surface ocean redox from iodine contents in ancient and recent carbonate. *Earth Planet. Sci. Lett.* **463**, 159–170.

Hayes C. T., Costa K. M., Anderson R. F., Calvo E., Chase Z., Demina L. L., Dutay J. C., German C. R., Heimbürger-Boavida L. E., Jaccard S. L., Jacobel A., Kohfeld K. E., Kravchishina M. D., Lippold J., Mekik F., Missiaen L., Pavia F. J., Paytan A., Pedrosa-Pamies R., Petrova M. V., Rahman S., Robinson L. F., Roy-Barman M., Sanchez-Vidal A., Shiller A., Tagliabue A., Tessin A. C., van Hulten M. and Zhang J. (2021) Global Ocean Sediment Composition and Burial Flux in the Deep Sea. *Global Biogeochem. Cycles* **35**, 1–25.

He Z., Archer C., Yang S. and Vance D. (2023) Sedimentary cycling of zinc and nickel and their isotopes on an upwelling margin : Implications for oceanic budgets and paleoenvironment proxies. *Geochim. Cosmochim. Acta* **343**, 84–97.

Higgins J. A., Blättler C. L., Lundstrom E. A., Santiago-Ramos D. P., Akhtar A. A., Crüger Ahm A. S., Bialik O., Holmden C., Bradbury H., Murray S. T. and Swart P. K. (2018) Mineralogy, early marine diagenesis, and the chemistry of shallow-water carbonate sediments. *Geochim. Cosmochim. Acta* **220**, 512–534.

Ho T. Y. (2013) Nickel limitation of nitrogen fixation in Trichodesmium. *Limnol. Oceanogr.* **58**, 112–120.

Holmden C., Kimmig S. R. and Nadeau M. D. (2024) Ca isotopic gradients in epeiric marine carbonates: Diagenetic origins of and significance for Ca cycle reconstructions. *Geochim. Cosmochim. Acta* **373**, 151–168.

Huang Y. and Fairchild I. J. (2001) Partitioning of Sr2+ and Mg2+ into calcite under karst-analogue experimental conditions. *Geochim. Cosmochim. Acta* **65**, 47–62.

Jarosch D. and Heger G. (1986) Neutron Diffraction Refinement of the Crystal Structure of

Aragonite. *Tschermaks Mineral. Pettrographische Mitteilungen* **35**, 127–131.

John S. G., Kelly R. L., Bian X., Fu F., Smith M. I., Nathan T., Liang H., Pasquier B., Seelen E. A., Holzer M. and Wasylenki L. (2022) The biogeochemical balance of oceanic nickel cycling. *Nat. Geosci.*

Kalderon-Asael B., Wang J., Planavsky N. J., Oehlert A. M., Vitek B. E., Reid R. P. and Tarhan L. G. (2024) Evaluation of early diagenetic signatures of lithium and stable strontium isotopes in shallow marine carbonate sediments. *Chem. Geol.* **676**.

Kelly R. L., John S. G., Cohen N. R., Hawco N. J., Pinedo-Gonzalez P., Lombard F., Bourdin G., Pesant S. and Gorsky G. (2022) *Tara Pacific Consortium (2022): Metal data collected during the Tara Pacific Expedition 2016-2018 [dataset]*., PANGAEA.

Kenter J. A. M., Ginsburg R. N. and Troelstra S. R. (2001) Sea-Level-Driven Sedimentation Patterns on the Slope and Margin. In *Subsurface Geology of a Prograding Carbonate Platform Margin, Great Bahama Bank: Results of the Bahamas Drilling Project* pp. 61–100.

Konhauser K. O., Pecoits E., Lalonde S. V., Papineau D., Nisbet E. G., Barley M. E., Arndt N. T., Zahnle K. and Kamber B. S. (2009) Oceanic nickel depletion and a methanogen famine before the Great Oxidation Event. *Nature* **458**, 750–753.

Konhauser K. O., Robbins L. J., Pecoits E., Peacock C., Kappler A. and Lalonde S. V. (2015) The Archean Nickel Famine Revisited. *Astrobiology* **15**, 804–815.

Kraus K. A. and Moore G. E. (1953) Anion Exchange Studies. VI.1,2 The Divalent Transition Elements Manganese to Zinc in Hydrochloric Acid. *J. Am. Chem. Soc.* **75**, 1460–1462.

Lakshtanov L. Z. and Stipp S. L. S. (2007) Experimental study of nickel(II) interaction with calcite: Adsorption and coprecipitation. *Geochim. Cosmochim. Acta* **71**, 3686–3697.

Lau K. V. and Hardisty D. S. (2022) Modeling the impacts of diagenesis on carbonate paleoredox proxies. *Geochim. Cosmochim. Acta* **337**, 123–139.

Lemaitre N., Du J., de Souza G. F., Archer C. and Vance D. (2022) The essential bioactive role of nickel in the oceans: Evidence from nickel isotopes. *Earth Planet. Sci. Lett.* **584**, 117513.

Li M., Grasby S. E., Wang S. J., Zhang X., Wasylenki L. E., Xu Y., Sun M., Beauchamp B., Hu D. and Shen Y. (2021) Nickel isotopes link Siberian Traps aerosol particles to the end-Permian mass extinction. *Nat. Commun.* **12**, 1–7.

Little S. H., Archer C., Mcmanus J., Najorka J., Wegorzewski A. V. and Vance D. (2020) Towards balancing the oceanic Ni budget. *Earth Planet. Sci. Lett.* **547**, 116461.

Liu X. M., Hardisty D. S., Lyons T. W. and Swart P. K. (2019) Evaluating the fidelity of the cerium paleoredox tracer during variable carbonate diagenesis on the Great Bahamas Bank. *Geochim. Cosmochim. Acta* **248**, 25–42.

Lorens R. B. (1981) Sr, Cd, Mn and Co distribution coefficients in calcite as a function of calcite precipitation rate. *Geochim. Cosmochim. Acta* **45**, 553–561.

Manfrino C. and Ginsburg R. N. (2001) Pliocene to Pleistocene Depositional History of the

Upper Platform Margin. In *Subsurface Geology of a Prograding Carbonate Platform Margin, Great Bahama Bank: Results of the Bahamas Drilling Project* pp. 17–39.

Marriott C. S., Henderson G. M., Crompton R., Staubwasser M. and Shaw S. (2004) Effect of mineralogy, salinity, and temperature on Li/Ca and Li isotope composition of calcium carbonate. *Chem. Geol.* **212**, 5–15.

Melim L. A., Swart P. K. and Maliva R. G. (1995) Meteoric-like fabrics forming in marine waters: implications for the use of petrography to identify diagenetic environments. *Geology* **23**, 755–758.

Melim L. A., Swart P. K. and Maliva R. G. (2001) Meteoric and Marine-Burial Diagenesis in the Subsurface of Great Bahama Bank. *Subsurf. Geol. a Prograding Carbonate Platf. Margin, Gt. Bahama Bank Results Bahamas Drill. Proj.* **70**, 137–161.

Melim L. A., Westphal H., Swart P. K., Eberli G. P. and Munnecke A. (2002) Questioning carbonate diagenetic paradigms: Evidence from the Neogene of the Bahamas. *Mar. Geol.* **185**, 27–53.

Milliman J. D. and Droxler A. W. (1995) Calcium Carbonate Sedimentation in the Global Ocean: Linkages Between the Neritic and Pelagic Environments. *Oceanography* **8**, 92–94.

Mills J. V., Barnhart H. A., DePaolo D. J. and Lammers L. N. (2022) New insights into Mn2+ and Mg2+ inhibition of calcite growth. *Geochim. Cosmochim. Acta* **334**, 338–367.

Murphy J. G., Ahm A. S. C., Swart P. K. and Higgins J. A. (2022) Reconstructing the lithium isotopic composition (δ7Li) of seawater from shallow marine carbonate sediments. *Geochim. Cosmochim. Acta* **337**, 140–154.

Murray S. T., Higgins J. A., Holmden C., Lu C. and Swart P. K. (2021) Geochemical fingerprints of dolomitization in Bahamian carbonates: Evidence from sulphur, calcium, magnesium and clumped isotopes. *Sedimentology* **68**, 1–29.

Nuester J., Vogt S., Newville M., Kustka A. B. and Twining B. S. (2012) The unique biogeochemical signature of the marine diazotroph Trichodesmium. *Front. Microbiol.* **3**, 1–15.

Oehlert A. M. and Swart P. K. (2019) Rolling window regression of δ 13 C and δ 18 O values in carbonate sediments: Implications for source and diagenesis . *Depos. Rec.* **5**, 613–630.

Oliveira L. and Antia N. J. (1986) Nickel ion requirements for autotrophic growth of several marine microalgae with urea serving as nitrogen source. *Can. J. Fish. Aquat. Sci.* **43**, 2427–2433.

Pichat S., Douchet C. and Albare F. (2003) Zinc isotope variations in deep-sea carbonates from the eastern equatorial Pacic over the last 175 ka. **210**, 167–178.

Pingitore N. E., Eastman M. P., Sandidge M., Oden K. and Freiha B. (1988) The coprecipitation of manganese(II) with calcite: an experimental study. *Mar. Chem.* **25**, 107–120.

Pogge von Strandmann P. A. E., Schmidt D. N., Planavsky N. J., Wei G., Todd C. L. and Baumann K. H. (2019) Assessing bulk carbonates as archives for seawater Li isotope ratios.

Chem. Geol. **530**, 119338.

Ragsdale S. W. (2009) Nickel-based enzyme systems. *J. Biol. Chem.* **284**, 18571–18575.

Ragsdale S. W. (1998) Nickel biochemistry. *Curr. Opin. Chem. Biol.* **2**, 208–215.

Ratié G., Jouvin D., Garnier J., Rouxel O., Miska S., Guimarães E., Cruz Vieira L., Sivry Y., Zelano I., Montarges-Pelletier E., Thil F. and Quantin C. (2015) Nickel isotope fractionation during tropical weathering of ultramafic rocks. *Chem. Geol.* **402**, 68–76.

Reeder R. J., Lamble G. M. and Northrup P. A. (1999) XAFS study of the coordination and local relaxation around Co2+ , Zn2+ , Pb2+ , and Ba2+ trace elements in calcite. *Am. Mineral.* **84**, 1049–1060.

Revels B. N., Rickli J., Moura C. A. V and Vance D. (2021) Nickel and its isotopes in the Amazon Basin : The impact of the weathering regime and delivery to the oceans. *Geochim. Cosmochim. Acta* **293**, 344–364.

Robbins L. J., Lalonde S. V., Planavsky N. J., Partin C. A., Reinhard C. T., Kendall B., Scott C., Hardisty D. S., Gill B. C., Alessi D. S., Dupont C. L., Saito M. A., Crowe S. A., Poulton S. W., Bekker A., Lyons T. W. and Konhauser K. O. (2016) Trace elements at the intersection of marine biological and geochemical evolution. *Earth-Science Rev.* **163**, 323–348.

Romaniello S. J., Herrmann A. D. and Anbar A. D. (2013) Uranium concentrations and 238U/235U isotope ratios in modern carbonates from the Bahamas: Assessing a novel paleoredox proxy. *Chem. Geol.* **362**, 305–316.

Rothman D. H., Fournier G. P., French K. L., Alm E. J., Boyle E. A., Cao C. and Summons R. E. (2014) Methanogenic burst in the end-Permian carbon cycle. *Proc. Natl. Acad. Sci. U. S. A.* **111**, 5462–5467.

Rudge J. F., Reynolds B. C. and Bourdon B. (2009) The double spike toolbox. *Chem. Geol.* **265**, 420–431.

Rue E. L., Smith G. J., Cutter G. A. and Bruland K. W. (1997) The response of trace element redox couples to suboxic conditions in the water column. *Deep. Res. Part I Oceanogr. Res. Pap.* **44**, 113–134.

Saenger C. and Wang Z. (2014) Magnesium isotope fractionation in biogenic and abiogenic carbonates: Implications for paleoenvironmental proxies. *Quat. Sci. Rev.* **90**, 1–21.

Schauble E. A. (2004) Applying stable isotope fractionation theory to new systems. *Rev. Mineral. Geochemistry* **55**, 65–111.

Schneider R. R., Schulz H. D. and Hensen C. (2000) Marine carbonates: Their formation and destruction. In *Marine Geochemistry* pp. 283–307.

Schönheit P., Moll J. and Thauer R. K. (1979) Nickel, cobalt, and molybdenum requirement for growth of Methanobacterium thermoautotrophicum. *Arch. Microbiol.* **123**, 105–107.

Sclater F. R., Boyle E. and Edmond J. M. (1976) On the marine geochemistry of nickel. *Earth Planet. Sci. Lett.* **31**, 119–128.

1158 Shannon R. D. (1976) Revised Effective Ionic Radii and Systematic Studies of Interatomic
1159 Distances in Halides and Chalcogenides. *Acta Crystallogr.* **32**, 751–767.

1160 Smith M. E., Moore E. W. and Swart P. K. (2022) Constraining diagenesis within shallow water
1161 carbonate environments: Insights from clumped and sulfur isotopes. *Chem. Geol.* **614**,
1162 121183.

1163 Spivak-Birndorf L. J., Wang S. J., Bish D. L. and Wasylenki L. E. (2018) Nickel isotope
1164 fractionation during continental weathering. *Chem. Geol.* **476**, 316–326.

1165 Strelow F. W. E. (1990) Distribution coefficients and cation-exchange behaviour of some
1166 ammines and aquo complexes of metallic elements in ammonium nitrate solution. *Anal.*
1167 *Chim. Acta* **233**, 129–134.

1168 Summerhayes C. P. and Thorpe S. A. (1996) Oceanography: an illustrated guide. *Oceanogr. an*
1169 *Illus. Guid.*

1170 Swart P. K. (2015) The geochemistry of carbonate diagenesis: The past, present and future.
1171 *Sedimentology* **62**, 1233–1304.

1172 Swart P. K. and Eberli G. (2005) The nature of the δ13C of periplatform sediments: Implications
1173 for stratigraphy and the global carbon cycle. *Sediment. Geol.* **175**, 115–129.

1174 Swart P. K. and Melim L. A. (2000) The Origin of Dolomites in Tertiary Sediments from the
1175 Margin of Great Bahama Bank. *SEPM J. Sediment. Res.* **Vol. 70 (2**.

1176 Swart P. K. and Oehlert A. M. (2018) Revised interpretations of stable C and O patterns in
1177 carbonate rocks resulting from meteoric diagenesis. *Sediment. Geol.* **364**, 14–23.

1178 Takano S., Tanimizu M., Hirata T., Shin K. C., Fukami Y., Suzuki K. and Sohrin Y. (2017) A
1179 simple and rapid method for isotopic analysis of nickel, copper, and zinc in seawater using
1180 chelating extraction and anion exchange. *Anal. Chim. Acta* **967**, 1–11.

1181 Takano S., Tsuchiya M., Imai S., Yamamoto Y., Fukami Y., Suzuki K. and Sohrin Y. (2021)
1182 Isotopic analysis of nickel, copper, and zinc in various freshwater samples for source
1183 identification. *Geochem. J.* **55**, 171–183.

1184 Tang J., Köhler S. J. and Dietzel M. (2008) Sr2+/Ca2+ and 44Ca/40Ca fractionation during
1185 inorganic calcite formation: I. Sr incorporation. *Geochim. Cosmochim. Acta* **72**, 3718–3732.

1186 Twining B. S., Baines S. B., Vogt S. and Nelson D. M. (2012) Role of diatoms in nickel
1187 biogeochemistry in the ocean. *Global Biogeochem. Cycles* **26**, 1–9.

1188 Veizer J., Fritz P. and Jones B. (1986) Geochemistry of brachiopods: Oxygen and carbon
1189 isotopic records of Paleozoic oceans. *Geochim. Cosmochim. Acta* **50**, 1679–1696.

1190 Wang C., Rybacki K., Hardisty D., Wang X., Reinhard C. T. and Planavsky N. (2021)
1191 Chromium Isotope Systematics and Diagenesis in Marine Carbonates. *Earth Planet. Sci.*
1192 *Lett.* **562**, 2711–2711.

1193 Wang R. M., Archer C., Bowie A. R. and Vance D. (2019) Zinc and nickel isotopes in seawater
1194 from the Indian Sector of the Southern Ocean: The impact of natural iron fertilization versus
1195 Southern Ocean hydrography and biogeochemistry. *Chem. Geol.* **511**, 452–464.

1196 Wang S.-J., Rudnick R. L., Gaschnig R. M., Wang H. and Wasylenki L. E. (2019)
1197 Methanogenesis sustained by sulfide weathering during the Great Oxidation Event. *Nat.*
1198 *Geosci.* **12**, 296–300.

1199 Watson E. B. (2004) A conceptual model for near-surface kinetic controls on the trace- element
1200 and stable isotope composition of abiogenic calcite crystals. *Geochim. Cosmochim. Acta* **68**,
1201 1473–1488.

1202 Wu G., Zhu J.-M., Wang X., Han G., Tan D. and Wang S.-J. (2019) A novel purification method
1203 for high precision measurement of Ni isotopes by double spike MC-ICP-MS. *J. Anal. At.*
1204 *Spectrom.* **34**, 1639–1651.

1205 Yang S. C., Hawco N. J., Pinedo-González P., Bian X., Huang K. F., Zhang R. and John S. G.
1206 (2020) A new purification method for Ni and Cu stable isotopes in seawater provides
1207 evidence for widespread Ni isotope fractionation by phytoplankton in the North Pacific.
1208 *Chem. Geol.* **547**.

1209 Yang S. C., Kelly R. L., Bian X., Conway T. M., Huang K. F., Ho T. Y., Neibauer J. A., Keil R.
1210 G., Moffett J. W. and John S. G. (2021) Lack of redox cycling for nickel in the water
1211 column of the Eastern tropical north pacific oxygen deficient zone: Insight from dissolved
1212 and particulate nickel isotopes. *Geochim. Cosmochim. Acta* **309**, 235–250.

1213 Zerkle A. L., House C. H., Cox R. P. and Canfield D. E. (2006) Metal limitation of
1214 cyanobacterial N2 fixation and implications for the Precambrian nitrogen cycle. *Geobiology*
1215 **4**, 285–297.

1216 Zhang S., Henehan M. J., Hull P. M., Reid R. P., Hardisty D. S., Hood A. v. S. and Planavsky N.
1217 J. (2017) Investigating controls on boron isotope ratios in shallow marine carbonates. *Earth*
1218 *Planet. Sci. Lett.*

1219 Zhao Z., Shen B., Zhu J. M., Lang X., Wu G., Tan D., Pei H., Huang T., Ning M. and Ma H.
1220 (2021) Active methanogenesis during the melting of Marinoan snowball Earth. *Nat.*
1221 *Commun.* **12**, 1–9.

1222